Idaho National Engineering Laboratory
Operated by the U.S. Department of Energy

Temperature Estimates from Zircaloy Oxidation Kinetics and Microstructures

Charles S. Olsen

October 1982

Prepared for the

U.S. Nuclear Regulatory Commission

Under DOE Contract No. DE-AC07-76IDO1570

EG&G Idaho

TEMPERATURE ESTIMATES FROM ZIRCALOY OXIDATION KINETICS AND MICROSTRUCTURES

Charles S. Olsen

Published October 1982

EG&G Idaho, Inc.
Idaho Falls, Idaho 83415

ABSTRACT

This report reviews state-of-the-art capability to determine peak zircaloy fuel rod cladding temperatures following an abnormal temperature excursion in a nuclear reactor, based on postirradiation metallographic analysis of zircaloy microstructural and oxidation characteristics. Results of a comprehensive literature search are presented to evaluate the suitability of available zircaloy microstructural and oxidation data for estimating anticipated reactor fuel rod cladding temperatures. Additional oxidation experiments were conducted to evaluate low-temperature zircaloy oxidation characteristics for postirradiation estimation of cladding temperature by metallographic examination. Results of these experiments were used to calculate peak cladding temperatures of electrical heater rods and nuclear fuel rods that had been subjected to reactor temperature transients. Comparison of the calculated and measured peak cladding temperatures for these rods indicates that oxidation kinetics is a viable technique for estimating peak cladding temperatures over a broad temperature range. However, further improvement in zircaloy microstructure technology is necessary for precise estimation of peak cladding temperatures by microstructural examination.

SUMMARY

Zircaloy microstructure and oxidation kinetics were comprehensively reviewed, and additional oxidation kinetic measurements were obtained at the Idaho National Engineering Laboratory (INEL) to establish the state-of-the-art capability for estimating—independently of thermocouple measurements—peak fuel rod cladding temperatures attained in nuclear reactors during abnormal temperature excursions. These temperature estimates will be used in light water reactor research programs to assess (a) the accuracy of thermocouple measurements of maximum fuel rod cladding temperatures from loss-of-coolant experiments (LOCEs), (b) the perturbation of the fuel rod cladding LOCE temperatures caused by the presence of thermocouples, and (c) cladding azimuthal temperature gradients near thermocouple locations.

A literature review revealed that cladding microstructure characteristics permit determination of whether peak cladding temperatures achieved during abnormal thermal transients are within the α phase (<1100 K), the $\alpha + \beta$ phase (1100 to 1240 K), or the β phase (>1240 K). At temperatures below 1240 K, determination of the transition temperature through identification of the allotropic phases from microstructures is imprecise because of uncertainties associated with the multiple transient history and effects of cooling rate upon the zircaloy microstructures. For temperatures above 1240 K, the β phase can be identified from the microstructure for different cooling rates expected during the LOCE. However, the actual temperatures may be determined within ±20 K from the fraction of β phase in the known two-phase $\alpha + \beta$ temperature region.

Cladding oxidation characteristics offer an alternative method to accurately estimate peak cladding temperatures over a broad temperature range. High-temperature (>1270 K) oxidation is well characterized as a function of temperature and time-at-temperature, and with existing data and experience peak cladding temperatures between 1270 and 1770 K can be inferred within an estimated uncertainty of ±40 to 70 K (95% confidence level), respectively.

For peak cladding temperatures below 1243 K, the limited oxidation data in the literature suggest that peak cladding temperatures in the high α and in the $\alpha + \beta$ region (970 to 1243 K) may be estimated by evaluating the extent of zircaloy oxidation. The current data in this temperature range were limited because (a) only one source of experimental data suitable for postirradiation examination (PIE) currently exists, and evaluation of potential systematic errors was not possible; (b) the data were not in a form which can be directly used for posttest metallographic analysis; and (c) the effect of multiple transients on oxidation characteristics was not evaluated.

Additional data for zircaloy oxidation rates in steam were obtained at INEL at temperatures of 961 to 1264 K and durations of 25 to 1900 s in order to overcome the above limitations and to calculate, in conjunction with measurements from postirradiation metallographic examinations, the prior peak temperatures of zircaloy fuel rod cladding in the $\alpha + \beta$ region. Additional results from oxidation tests conducted by other laboratories were used to validate the current INEL data base in the two-phase $\alpha + \beta$ temperature region.

Zircaloy oxidation rates determined at INEL were applied to a zircaloy-clad electrical heater rod that had been subjected to four transients and to three nuclear fuel rods that had variously been subjected to from one to four transients in the $\alpha + \beta$ temperature region. The calculated temperatures near three external thermocouples on the electrical heater rod were higher than the measured values by 16 to 34 K. Measurements of the oxide thickness indicated that a peak temperature of 1191 K occurred between the two external thermocouples which implies an azimuthal temperature gradient of ~50 K. Good agreement between calculated and measured temperatures was also obtained for the nuclear fuel rods tested under transient conditions.

Zircaloy microstructure and oxidation kinetics provide two independent techniques for estimating peak cladding temperatures. Zircaloy microstructures can be used to estimate temperature ranges, but improvement in microstructure technology is required to estimate detailed temperatures even in the $\alpha + \beta$ temperature region. Oxidation kinetics can be used to estimate peak cladding temperatures over a broad temperature range, and the required assumption of time at temperature has an insignificant effect on the results.

CONTENTS

TEMPERATURE ESTIMATES FROM ZIRCALOY OXIDATION KINETICS AND MICROSTRUCTURES

INTRODUCTION

This report reviews and summarizes state-of-the-art capability to determine peak fuel rod cladding temperatures from posttest metallographic analysis of zircaloy microstructure and oxidation characteristics. The results of a comprehensive literature search are presented to evaluate the adequacy of available zircaloy microstructures and oxidation data for accurately estimating expected LOFT peak cladding temperatures. Based upon this review, additional oxidation measurements were performed to further evaluate and characterize low-temperature zircaloy oxidation for posttest metallographic applications. The oxidation results in conjunction with microstructures are evaluated to estimate prior peak zircaloy cladding temperatures.

Cladding temperatures during thermal transients are the primary means for determining the effectiveness of Emergency Core Cooling Systems (ECCS) and to ensure that the core will remain in a coolable geometry. Two ECCS criteria[1] for light-water-cooled nuclear power reactors were established in December 1973 to ensure the integrity of the cladding during a loss-of-coolant-accident (LOCA). One criterion states that maximum cladding temperature shall not exceed 1478 K (2200°F). The second criterion limits the total oxidation of the cladding (in the form of ZrO_2) to 0.17 times the original cladding thickness. The first criterion is based upon temperature alone, but the latter incorporates, through cladding oxidation, time at temperature in addition to temperature. These criteria establish the importance of reliably determining cladding temperatures during loss-of-coolant experiments (LOCEs).

Cladding temperatures are also the most important single measurement for evaluating fuel rod models that predict the thermal-mechanical response of the cladding and for estimating the

fuel rod-to-coolant heat transfer, which is required to evaluate the analytical models that predict subchannel thermal-hydraulic response. At the Loss-of-Fluid-Test (LOFT) facility at the Idaho National Engineering Laboratory (INEL), cladding surface temperatures are measured by thermocouples attached to the cladding surface. The measured cladding surface temperature, however, can be different from the true cladding surface temperature as a result of perturbations in the cladding surface geometry and potential selective cooling of the thermocouple as a result of its protrusion into the coolant channel. Biederman[2] indicated that for steady-state power and flowing steam, measured cladding temperatures were 100 K lower than true temperatures. During Power Burst Facility (PBF) tests[3-8] characterized by high steady linear heat generation rates (49.2 to 65.6 kW/m) in film boiling conditions, measured cladding temperatures were lower than the true temperatures (estimated from posttest metallurgical evaluations) by 100 to 300 K. Although these temperature perturbations may not be typical for the LOFT transient (low-heat flux conditions for the LOCE), these results suggest some perturbation of the true cladding temperature caused by surface thermocouples.

Because postirradiation examinations (PIE), which include metallographic analysis of the cladding microstructure and oxidation characteristics, offer a means of determining peak cladding temperature independent of thermocouple measurements, these techniques were evaluated for the capability to assess maximum cladding temperatures. PIE techniques provide nuclear safety testing a means to (a) verify peak cladding thermocouple measurements, (b) determine the perturbation of fuel rod cladding temperature history caused by the presence of thermocouples, and (c) determine cladding azimuthal temperature gradients near the thermocouple locations.

METALLURGICAL TECHNIQUES FOR EVALUATING CLADDING TEMPERATURES

Zircaloy microstructures are sufficiently different among the allotropic phases (α, $\alpha + \beta$, and β) to permit microstructures to be correlated with temperatures. Measurement of the extent of oxidation (oxide layer thickness or weight gain) allows an exact evaluation of cladding temperatures. State-of-the-art techniques for using both zircaloy microstructures and oxidation to determine peak cladding temperatures are summarized in the following sections.

Zircaloy Microstructures

Since zircaloy phase transformation is dependent upon the solutes Ni, Cr, Fe, Sn, O, and H, transition from the α phase to β phase occurs over a temperature range rather than at a single temperature.[9-11] Experimental data for hydrogen-free zircaloy show that the temperature range for transformation from α to β zircaloy is 1103 to 1243 K.[11] In addition, zircaloy recrystallization has been shown to initiate at 866 K. The resulting grain structure is readily distinguishable from the cold-worked microstructure (see Appendix A). In principle, these zircaloy microstructural characteristics can be correlated with cladding temperature ranges (as shown in Table 1) and used to determine peak cladding temperatures by metallographic techniques.

Identification of the cold-worked versus annealed microstructure presents no problem, and the β phase microstructures can be readily identified for cooling rates above 2 K/s since they exhibit a readily identifiable acicular (needle-like) or platelet grain shape.[12-15] The α and the $\alpha + \beta$ phases have a more equiaxed grain shape than the β phase grains. Identification of the β phase has been used in tests conducted in the PBF program to establish peak cladding temperatures over 1243 K, but the need to rely upon the low-temperature microstructures did not exist for these tests.[3-8] For the LOCA-11[16] and LOFT Lead Rod Tests[17] in PBF, cladding temperatures were below 1243 K, and low-temperature metallurgical techniques were required to estimate these lower temperatures.

Certain problems exist in distinguishing two-phase, $\alpha + \beta$ zircaloy from single-phase α zircaloy in etched samples and consequently, in identifying the onset of the α to $\alpha + \beta$ transition. For cooling rates above 5 K/s, both the α and $\alpha + \beta$ phases exhibit nearly identical equiaxed grain structures (see Appendix A) and the microstructures change markedly with different cooling rates.[12,18-20] Intermetallic precipitation occurs predominantly in the grain boundaries in the $\alpha + \beta$ phase region when slowly cooled at the rate of about 1 to 2 K/s. At rates faster than 10 K/s, these precipitates either do not form or they are too small to be discernible with a light microscope (see Appendix A). The morphology of these precipitates offers a potential means of identification of the two-phase region, but their absence does not preclude identification of temperatures in the two-phase region. The morphology of α cores in a transformed β matrix

Table 1. Cladding temperature ranges for zircaloy crystallographic phase transitions

Transition	Transition Temperature (K)	Identified Phase	Temperature Range (K)
Recrystallization	866	Cold worked	>866
α to $\alpha + \beta$	1103	Annealed	866 to 1103
$\alpha + \beta$ to β	1243	$\alpha + \beta$	1103 to 1243
		β	>1243

offers a more positive identification than that of the precipitates, but the use of this morphology is doubtful at temperatures near the transition temperatures of the two-phase region because very low amounts of the β phase at the lower transition temperature or the α phase at the higher transition temperature may not be identifiable.

Although current published microstructure data applicable to LOCE transients do not substantiate the use of microstructures to estimate temperatures within each phase region, the possibility exists that microstructure data, reflecting cooling rate effects, etc., could be used to estimate temperatures within the $\alpha + \beta$ phase based upon the phase diagram lever rule and the fraction of α phase. Temperatures may be estimated within ± 20 to ± 30 K using the fraction of α phase and the transition temperatures. Presently, no metallographic procedure provides usable contrast between the α and β phases, and the results of current methods are extremely dependent upon human skills to estimate the fraction of α phase present.

Zircaloy Oxidation

Zircaloy reacts with steam to form ZrO_2 and a solution of oxygen in zirconium to form different reaction layers.[15] Experimental data were obtained to characterize the extent of oxidation as a function of temperature and reaction time (time-at-temperature) for temperatures above 973 K.[15,21-30] The extent of oxidation is determined either by weight gain or reaction layer thicknesses. For convenience, the experimental data are categorized as either high-temperature (>1270 K) or low-temperature (900 to 1270 K) oxidation in the following discussions.

High-Temperature Oxidation Data. Zircaloy oxidation rates have been investigated for isothermal conditions above 1270 K[15,21-26] from which Cathcart's data[15] are accepted as the most comprehensive and reliable. Extreme care was taken to calibrate thermocouple response in-situ and correlate oxidation extents with precise locations of the verified thermocouple measurements. Extent of oxidation was characterized for durations up to 2000 s by total weight gain and by three kinetic correlations for reaction layer thicknesses.

Analytical models were developed to correlate this isothermal data with temperature and the square root of time for subsequent application to transient temperature conditions.[15] The details of the four correlations are given in Appendix B. The correlation based upon the thickness of the oxide plus oxygen-stabilized α zircaloy layers, which is directly applicable to PIE, results in errors in estimated temperatures of 40 to 70 K (95% confidence level). (See Appendix C for details.) This correlation has been extensively applied to evaluate peak cladding temperatures during PBF tests in which cladding temperatures exceeded 1273 K.[3-8]

The extent of oxidation measured after temperature transients was first shown by Biederman[21] and then by Cathcart[15] to be substantially less than that predicted by models derived from isothermal data. From limited data between 1323 and 1673 K, this transient effect was found to predominate between 1323 and 1473 K. The cause of this anomalous behavior is attributed to the transformation from tetragonal to monoclinic oxide of zirconium. Isothermal data are often applied to transient problems,[31] but care must be taken to ensure that transients do not introduce additional phenomena not represented by steady-state data. Additional transient data and further evaluation will be required to develop the application of isothermal data to transient conditions.

Other published data[21-24] significantly differ from Cathcart's. The extrapolation of the Baker-Just correlation[22-24] [based upon a few data points at the zircaloy melting point and verified by Special Power Excursion Reactor Test (SPERT) tests[32] at the zircaloy melting point] to lower temperatures is approximately a factor of two higher than Cathcart's correlation. Extrapolation of the Baker-Just correlation to temperatures below the zircaloy melting point is not justified. Biederman's reaction layer thicknesses[21] are a factor of two less than Cathcart's reaction layer thicknesses[15] and the differences are attributed to poor temperature measurements. The discrepancy between Biederman's and Cathcart's data emphasizes the importance of accurate experiment characterization for all temperatures.

Low-Temperature Oxidation Data. Isothermal oxidation data between 973 and 1273 K and at atmospheric pressure were obtained from Leistikow[33] and limited data from Pawel[27] in this temperature range for pressures up to 10.34 MPa were combined with those from Leistikow. Leistikow determined the oxidation extent

gravimetrically so that the total oxygen weight gain (mg/cm^2) is correlated with temperature and time. The Pawel oxygen weight gain data were derived from thickness measurements by using computer codes.

Leistikow's data followed parabolic kinetics near 1200 K, but became increasingly cubic as the temperature decreased. Pawel's data also exhibited cubic kinetics at the high steam pressures. On the other hand, Leclercq's[30] data at low oxygen or steam pressures (<100 kPa) also exhibited cubic kinetics. In contrast, data from Biederman and Urbanic in this temperature region exhibited parabolic kinetics. Biederman's data exhibited temperature measurement errors, and Urbanic's data is based only upon oxygen uptake and is not amenable to PIE.

The data base in the intermediate-temperature region is contradictory, and is subject to systematic errors as observed with the high-temperature Biederman data.[21] Additional data are required to evaluate systematic errors in the present data in this temperature range. The gravimetric tests conducted at Chalk River Nuclear Laboratory, with the emphasis on studying the effect of oxidation upon the α to β zircaloy phase transformation, did not include oxide thickness measurements which are required for PIE. Evaluation of the systematic errors in thickness measurements can be performed through comparison of weight gain measurements from Urbanic and Biederman, but these data are not sufficient to develop an oxidation model in the $\alpha + \beta$ temperature region. The additional oxide-thickness and weight-gain data required are discussed in the next section.

Discussion. Metallurgical examination of zircaloy cladding during PIE offers two independent techniques for estimating cladding temperatures. The first technique, based upon zircaloy microstructures, permits determination of a temperature range through identification of allotropic phases and knowledge of the transition temperatures; however, problems exist in distinguishing the α and $\alpha + \beta$ phases at different cooling rates. For cooling rates above 2 K/s expected during LOCEs, the β phase can be readily identified. The potential exists for determining temperatures within ±20 K (see Appendix A) from the fraction of α phase. Microstructure, as a temperature measurement device, has the advantage that knowledge of time at temperature is not required.

The second technique, based upon measurement of reaction layer thicknesses and correlations for oxidation kinetic rates, can be used to estimate cladding temperatures but requires knowledge of the time at temperature. The microstructure can also be used to select the appropriate kinetic equations for the temperature regions involved.

The isothermal oxidation data above 1273 K are well characterized and provide a means for determining peak cladding temperatures within ±60 K (95% confidence level) using Cathcart's model to evaluate oxide layer thicknesses. Limited transient data between 1323 and 1473 K suggest that a problem exists in extrapolating isothermal oxidation data to transient conditions.

Low-temperature oxidation data available in the literature are not consistent, and the more reliable data from Chalk River are not amenable to PIE. Additional data, in terms of oxygen uptake at low temperatures, are required to validate new data and measurements of oxide layer thickness are required for PIE evaluations.

OXIDATION RATES IN $\alpha + \beta$ PHASE TEMPERATURE REGION

Review of the available literature presented in the appendixes and summarized in the previous sections indicated that additional oxidation data were required.

Oxidation experiments conducted at INEL are described in the following sections.

Experimental Procedure

Zircaloy-4 nuclear-grade tubing was manufactured by Sandvik Special Metal Corporation according to commercial specifications used for LOFT fuel rods. As part of the commercial specification, the tubes were "pickled" to remove about 0.038 mm of material from the outside surface. The tubing has an outside diameter of 10.72 mm, a thickness of 0.601 mm, and a length of ~180 cm.

Oxidation samples 2.3 cm long were cut from the tubes. No further etching or other surface treatment occurred, so oxidation results were representative of beginning-of-life tubing and tubing manufactured to current commercial practice. The samples were measured for length, degreased, and weighed immediately prior to use. Certified chemical analyses of major elements in this tubing alloy indicated 1.60% Sn, 0.21% Fe, 0.11% Cr, 47 ppm Ni, 1210 ppm O, and 45 ppm N.

The test facility used to oxidize the zircaloy-4 samples in steam consisted of a steam generator and superheater, a condensing system, a reaction chamber, and a furnace (Figure 1). In addition to the pre- and posttest weight measurements, in-situ weight measurements were performed in the reaction chamber using a quartz spring and a Gaertner Model M303p cathetometer. The quartz spring was contained in a water-cooled chamber, with access to the chamber restricted to a diameter only slightly larger than the diameter of the quartz fiber holding the sample in order to minimize the entry of steam into the chamber. A small flow (~2 cc/min) of helium, introduced at the top of the water cooled jacket, flowed down through the reaction chamber to inhibit steam flow into the chamber containing the quartz spring.

Saturated steam, produced from demineralized water in a three-necked flask heated with a 1200-W Glas-Col heater, was superheated to the desired temperature, passed through the reaction chamber, and finally to a condenser. A steam flow of 20 g/min was established by the power of the Glas-Col heater. The glass tubing carrying the steam to the top of the reaction vessel was wrapped with electric heat-tape and insulated. The temperature of the tubing was monitored using two digital indicators at four equidistant positions between the flask and the entry into the furnace.

An in-situ calibration was performed to determine the axial temperature profile in the furnace in order to establish the location and length of the hot zone. A "chimney" effect in the furnace moved the hot zone above the midpoint of the furnace, but the flow of steam down through the furnace shifted the hot zone below the furnace center (Figure 2). The furnace was moved vertically to position the sample in the hot zone after the steam flow was established to start the reaction, and removed from around the sample to quench the sample in steam.

The furnace temperature was controlled proportionately by a Love Model 1961 silicon-controlled power supply using the difference between measured and set temperatures. Furnace temperature was measured by a Type K, Chromel-Alumel thermocouple.

The sample temperature was measured using a 1.59-mm-OD, stainless steel sheathed, Chromel-Alumel thermocouple, positioned in the center of the sample but not attached to the sample because of the requirement for in-situ weight measurements. Sufficient clearance was provided to allow the passage of steam through and around the sample. A few tests were performed with a thermocouple spot-welded to the inside of the cladding; the heating and cooling rates were about 10 K/s faster than the 3-K/s rate of the unattached thermocouple, but no differences in peak temperature were noted. An example of the temperature cycle is shown in Figure 3.

After oxidation, each specimen was weighed and sectioned in the transverse plane, mounted, polished, and etched for metallographic examination. The oxide layer formed on the cladding surface, with a layer of oxygen-rich zirconium
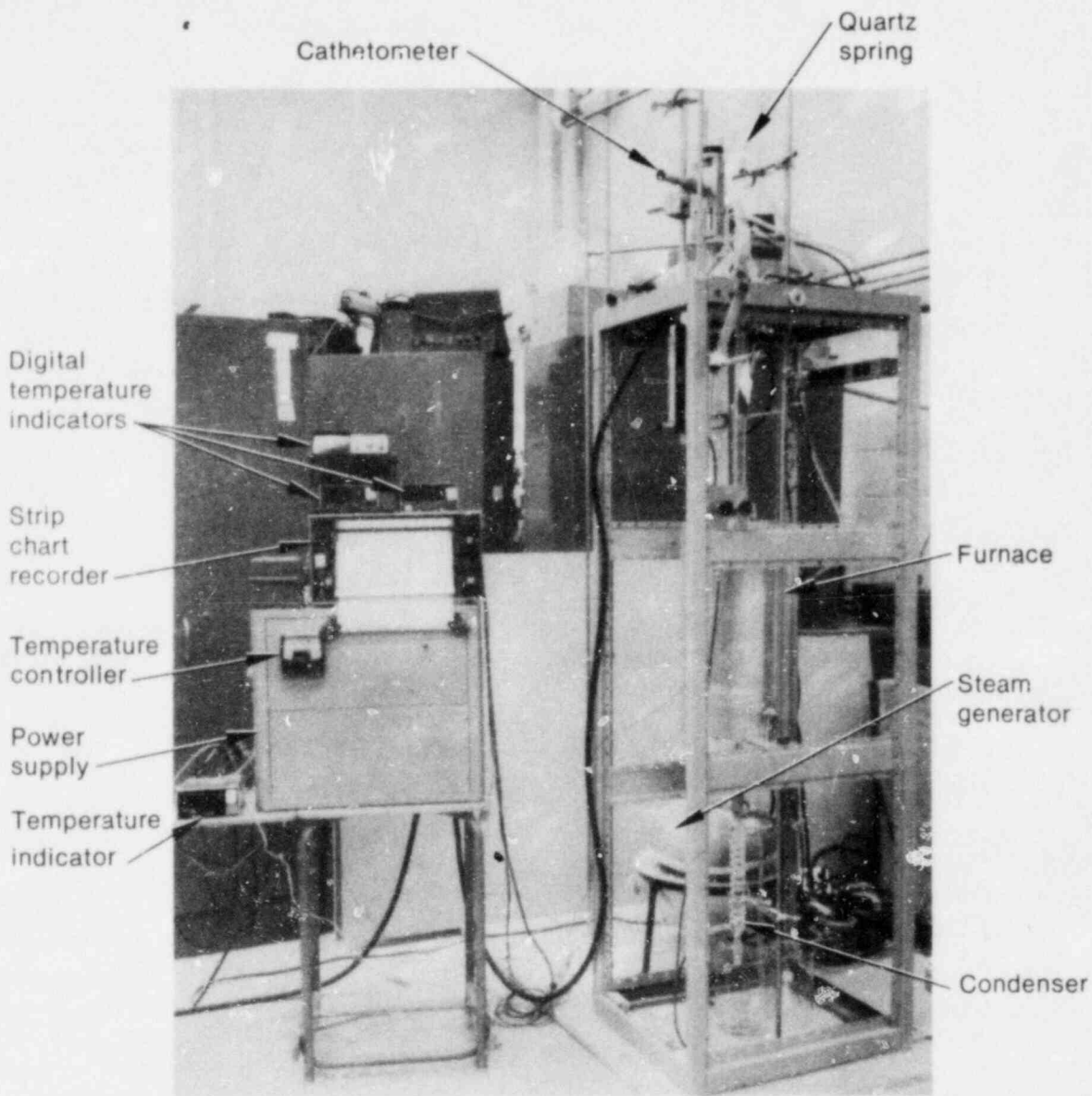
Figure 1. Zircaloy oxidation test apparatus.

Results and Discussion

adjacent to the oxide layer caused by oxygen diffusion into the base metal. The total thickness of the layers was measured, and the weight gain was determined from the difference between pre- and posttest weight measurements. The weight gain per unit area was calculated from the inside and outside diameters of the cladding.

A total of 108 samples was used in the temperature range of 961 to 1263 K and for effective times ranging from 1 to 30 min. Effective times were calculated from the average isothermal temperature to compensate for heating and cooling times, using the exponential Arrhenius equation.

The in-situ weight measurements offer an almost continuous source of weight gain measurements versus time for a given sample and temperature. With this method, the number of samples could be reduced and the variability in sample temperature eliminated. However, in order to supply sufficient quantities of steam and avoid steam starvation, the risk of condensation compromising the weight measurements exists. The results of this technique and those of the alternative of using separate samples for each temperature and time
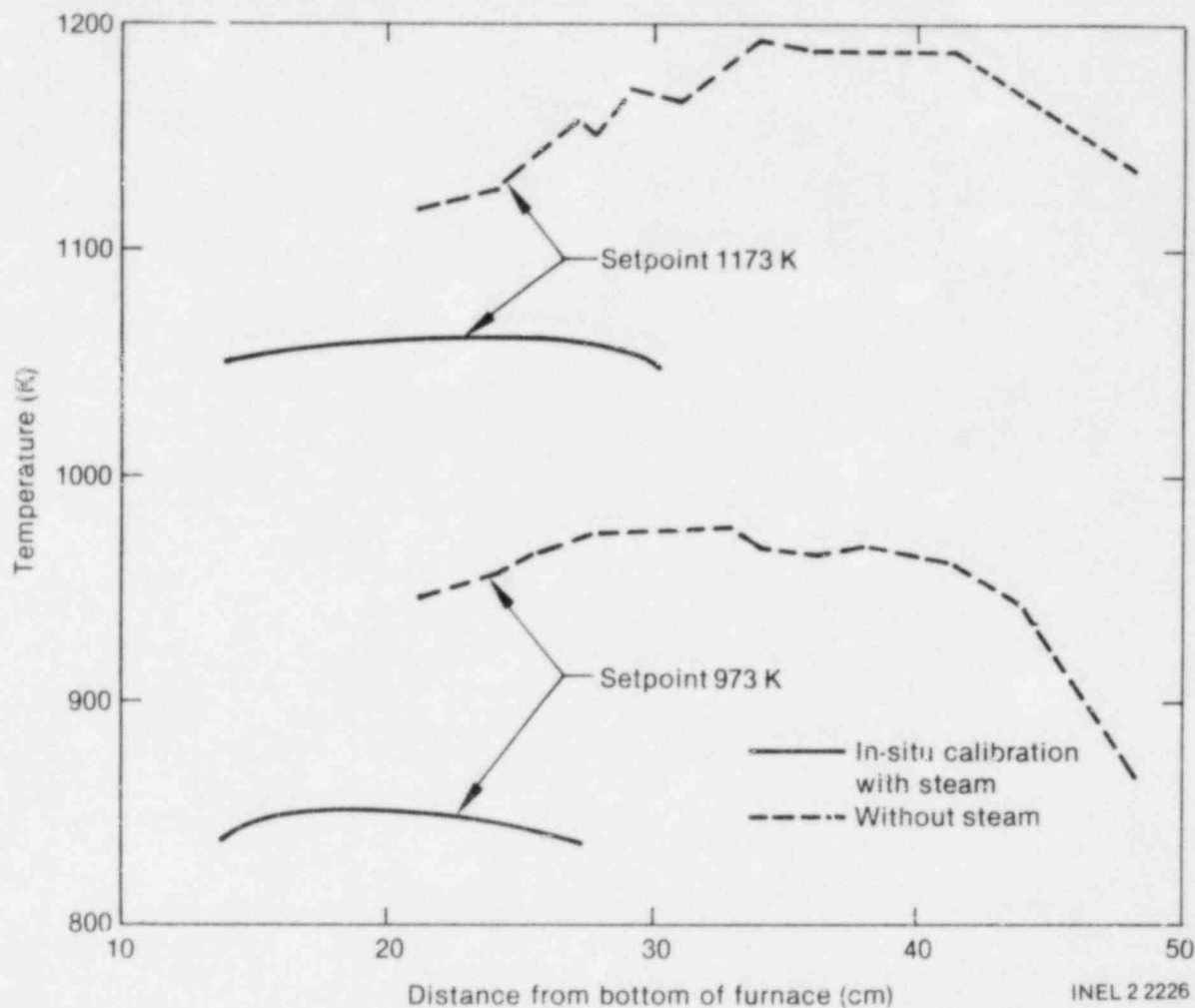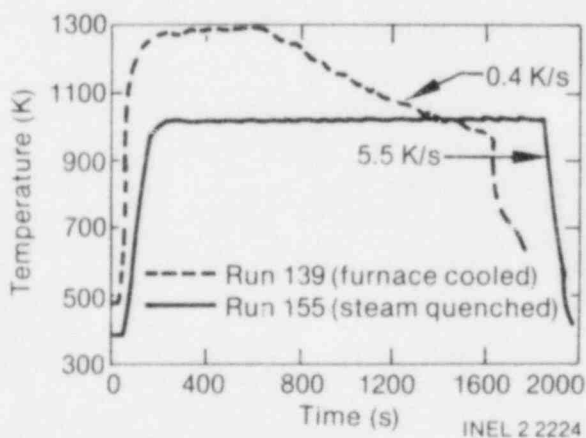
Figure 2. Furnace axial temperature profile.

Figure 3. Typical temperature-time profiles for zircaloy oxidation.

combination and the results of the layer thickness measurements are discussed in the following two subsections.

Oxygen Uptake. The weight gain measurements derived from the differences in pre- and posttest weight gain are shown in Figure 4 as a function of the square root of time for different temperatures. Within experimental error, parabolic kinetics are indicated by the linear relationship exhibited in Figure 4.

An alternative method of examining this data is to determine the exponential coefficients. These values are listed in Table 2 with their standard deviation. The values range from 0.39 to 0.59 with only one value (1168 K) below 0.33. Within
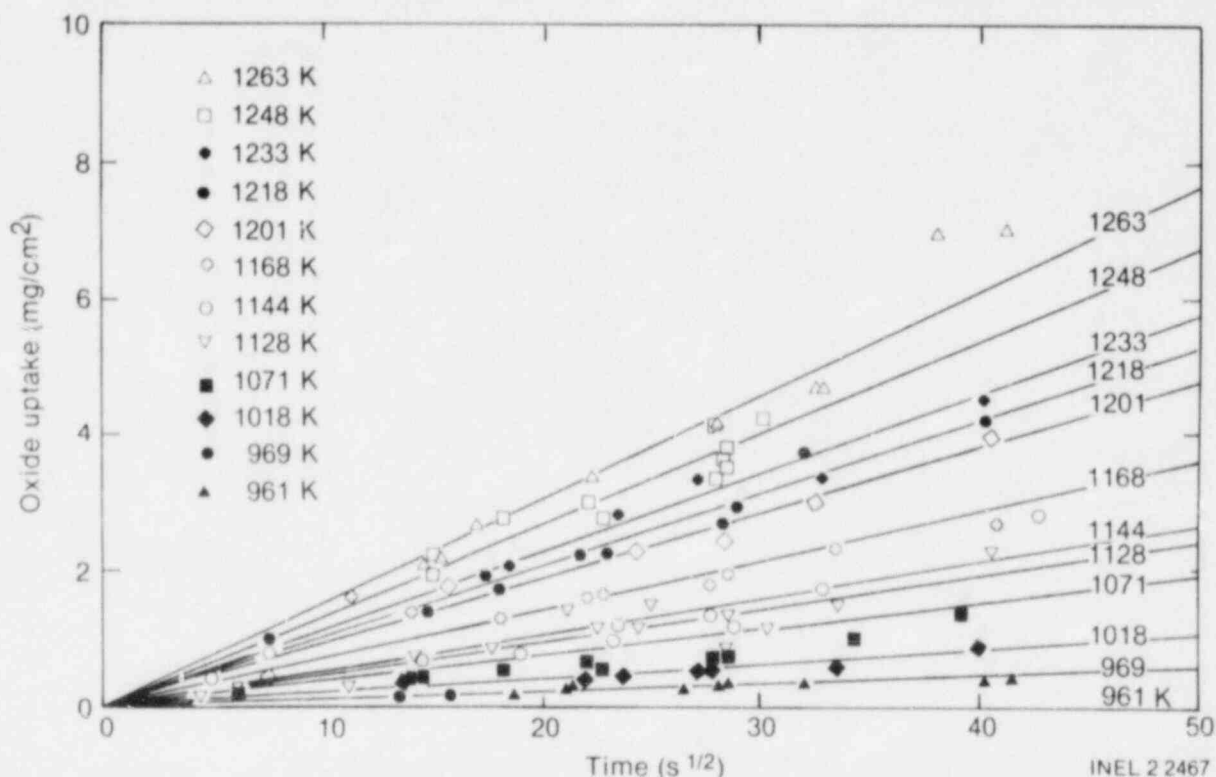
Figure 4. Oxygen uptake as a function of time for different temperatures.

Table 2. Exponential coefficients from pre- and posttest weight measurements

Temperature (K)	Coefficient	Standard Deviation
1263	0.5826	0.1621
1248	0.4401	0.0501
1233	0.3905	0.0544
1218	0.4634	0.0285
1201	0.5234	0.0791
1168	0.3066	0.0514
1144	0.4245	0.05264
1128	0.5905	0.0705
1071	0.4571	0.0365
1018	0.4271	0.0480
969	0.8948	0.0769
961	0.4126	0.0810

the experimental error of the data, the weight gain measurements obey the parabolic rate law.

The temperature dependence of the parabolic rate constant for oxygen uptake is shown in Figure 5 for the temperature range between 1000 and 1250 K. This temperature dependence is represented by Equation (1), and the errors in the constants represent one standard deviation.

$$k_w = 479.02 \begin{pmatrix} +23.3\% \\ -28.9\% \end{pmatrix} \exp\left[-20\ 400(\pm 2.3\%)/RT\right]$$

(1)

where

k_w = parabolic constant for weight gain ($Mg\ O/cm^2 \cdot s^{1/2}$)

R = 1.987 cal/mole·K
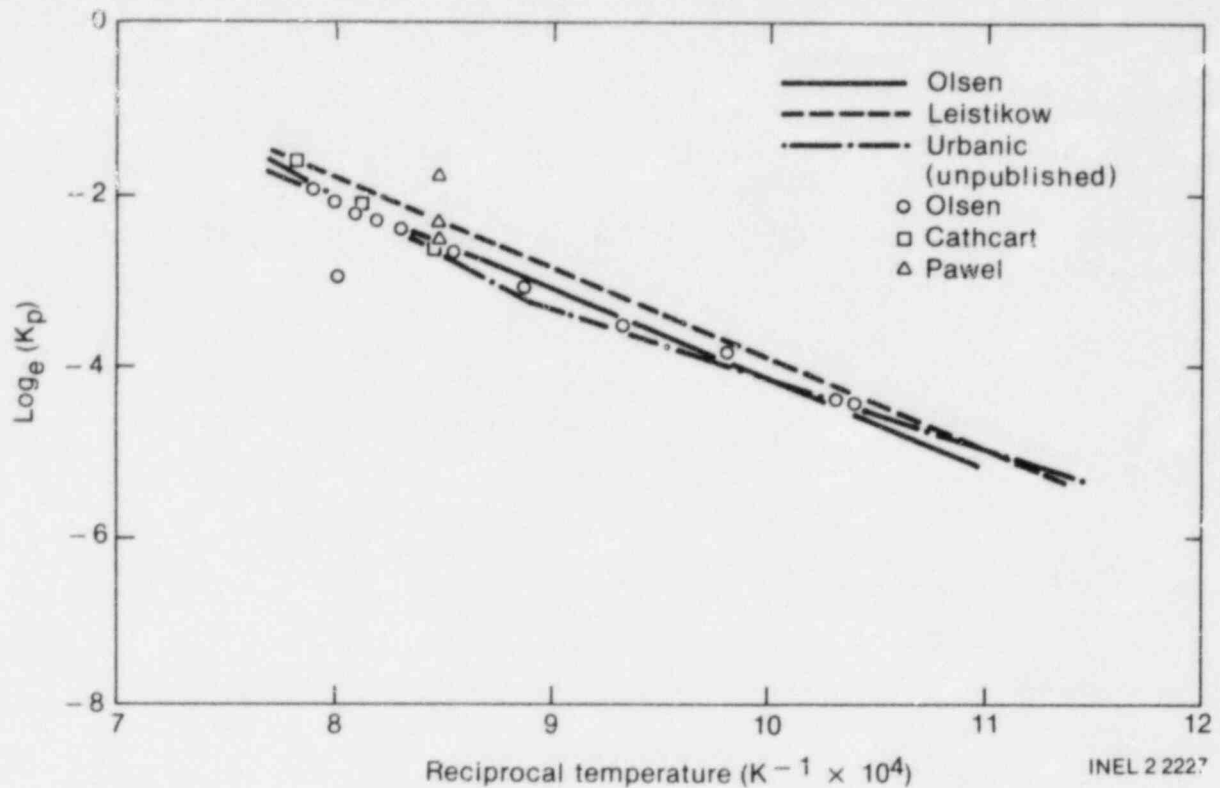
T = temperature (K).

8

Figure 5. Temperature dependence of parabolic rate constant for oxygen uptake.

The data are compared with results from Leistikow,[33] Cathcart,[15,27] and unpublished results from Urbanic in Figure 5. Urbanic chose to differentiate the kinetics between the single α phase temperature region and the two-phase $\alpha + \beta$ temperature region. The data agree well with Urbanic's and Cathcart's data; Leistikow's data are higher than both. Leistikow combined data from the β phase temperature region and the two-phase $\alpha + \beta$ temperature region, but his low-temperature data exhibited increasing cubic kinetics with decreasing temperature.

Three data points from Pawel for high-pressure steam at 3.45, 6.90, and 10.34 MPa are compared with the INEL data in Figure 5. The values at 3.45 and 6.90 MPa exhibit cubic kinetics. The values at 10.34 MPa are higher and exhibit parabolic kinetics. These differences suggest a pressure effect on the oxidation kinetics.

The weight gain measurements from the cathetometer were more scattered than those from the pre- and posttest measurements. Figure 6 compares the weight gain measurements from the cathetometer for a single sample at 873 K with that of pre- and posttest measurements for several samples at an average temperature of 871 K. Less scatter exists in the cathetometer data but bias exists in the data due to steam condensation, temperature variations when the furnace is moved, and transient temperature around the quartz spring.

Oxide Layer Thickness. Oxide layer thickness measurements in the two-phase $\alpha + \beta$ temperature region include an oxygen-rich layer adjacent to the oxide layer, so most of the oxygen can be accounted for in the oxide thickness measurement (Figure 7). The oxide/oxygen-rich layer was more difficult to resolve than the oxygen-rich/metal interface. The oxide thicknesses from the outside and inside surfaces were combined in deriving the parabolic rate constants for different temperatures.

The oxide thickness measurements are shown in Figure 8 as a function of the square root of time for different temperatures. The growth of the oxide layer, as with oxygen uptake, follows the parabolic oxidation rate law.
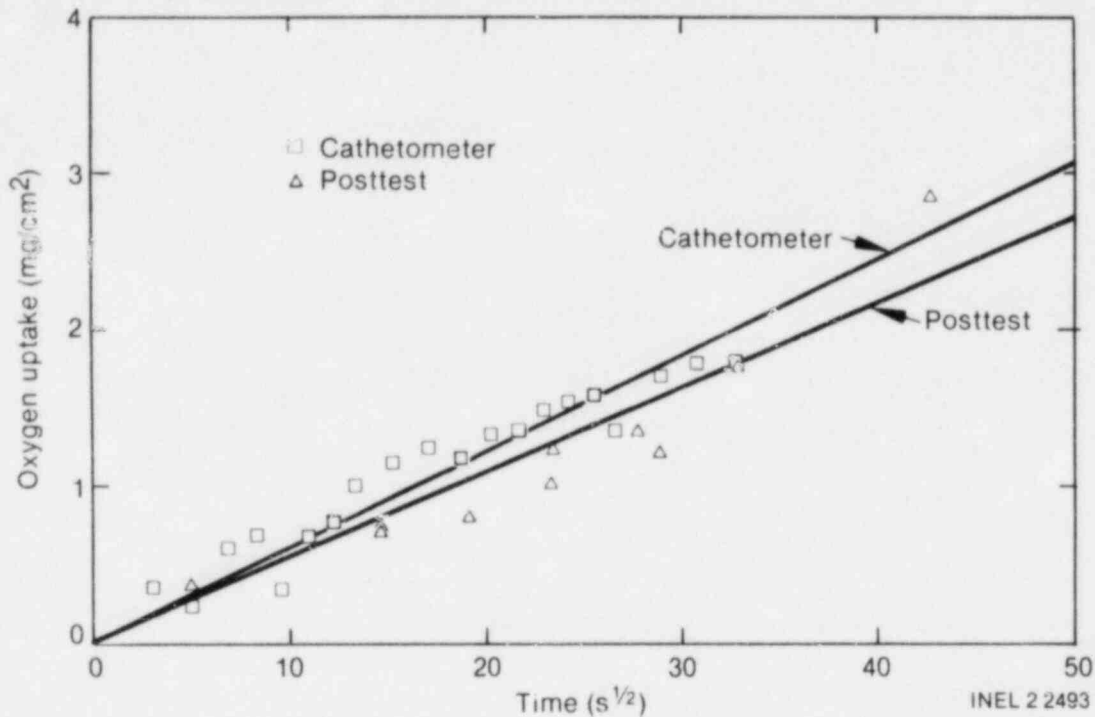
9

Figure 6.   Comparison of oxygen uptake from cathetometer and pre- and posttest weight measurements.

The temperature dependence of the parabolic rate constants for oxide layer growth is shown in Figure 9 and can be represented by Equation (2). The errors represent one standard deviation.

$$k_o = 2.526 \times 10^4$$

$$\left(\begin{array}{c} +38.5\% \\ -27.8\% \end{array} \right) \exp \, [-23\,920(\pm 3.1\%)/RT] \quad (2)$$
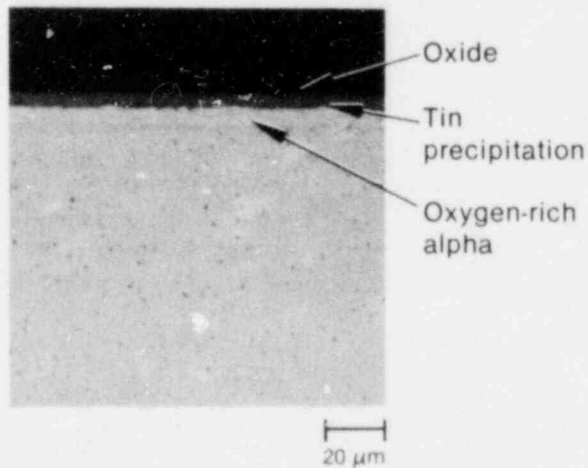
where

k_o = oxide layer parabolic rate constant $(\mu m/cm^2 \cdot s^{1/2})$.

The data are compared with results from Leistikow,[33] Pawel,[27] and Biederman[21] in Figure 9. Leistikow's data, as with his oxygen uptake data and Biederman's data, are above those of INEL and Cathcart. Biederman separated his data into two temperature intervals from 922 to 1144 K and from 1172 to 1227 K, intervals approximating the α and $\alpha + \beta$ phase temperature regions, as with Urbanic's oxygen uptake data. The oxygen uptake and oxide layer data do not substantiate different oxidation rates in this temperature interval.

The oxygen uptake data were compared with other data in the literature to establish the validity of the procedure and equipment, since weight gain measurements are normally more precise than layer thickness measurements. With the agreement obtained with oxygen uptake data, the validity of the layer-thickness measurements is established since the same samples are used for both oxygen uptake and layer thickness measurements.

Figure 7.   Oxide layer growth at 1072 K for 1072 s.
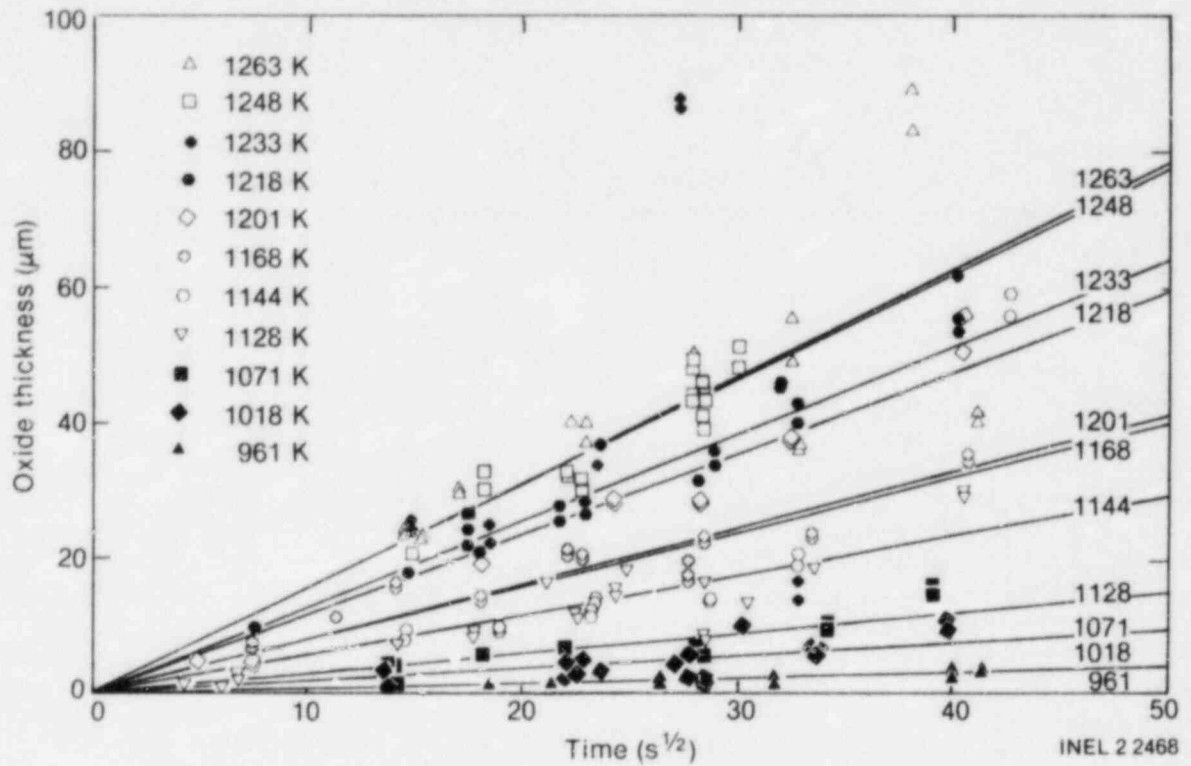
10

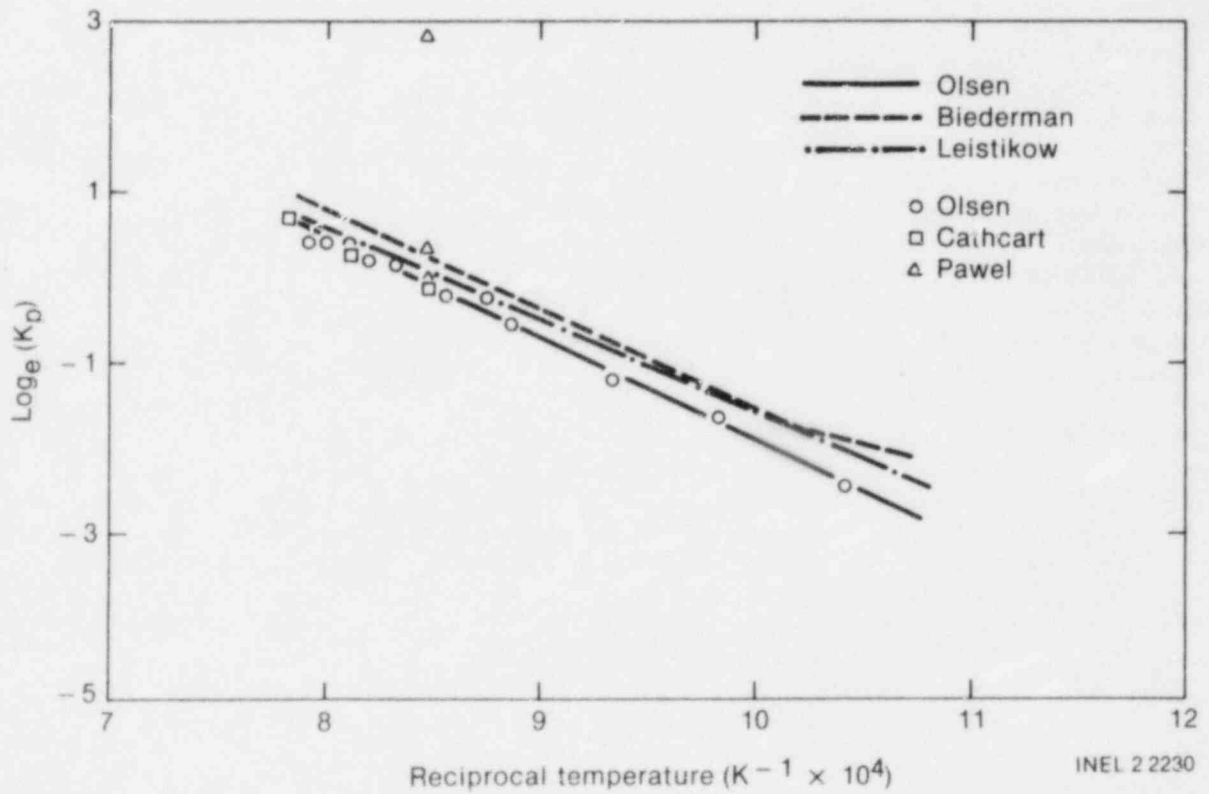Figure 8.   Oxide layer growth as a function of time for different temperature.

Figure 9.   Temperature dependence of parabolic rate constant for growth of oxide plus oxygen-rich layers.

11

TEMPERATURE ESTIMATES FROM ZIRCALOY
OXIDATION KINETICS

The oxidation kinetics of zircaloy were reviewed and out-of-pile tests were performed to improve the data base. In this section the application of oxidation kinetics to estimation of prior peak cladding temperatures is evaluated for different conditions.

Samples from the isothermal oxidation tests in the $\alpha + \beta$ temperature region were selected to compare measured temperatures with those calculated from the oxidation kinetics and the temperature-time profiles in order to estimate the random error in these estimates and compare these errors with those estimated from linear error propagation theory (see Appendix C). In addition, prior peak temperatures were estimated using oxidation kinetics from PIE of one electrical heater rod[34] and three nuclear fuel rods tested under LOCE conditions[17] and three nuclear fuel rods tested under power-coolant mismatch (PCM) conditions[4] for an evaluation of this technique under nonisothermal conditions.

The temperature estimates for the prior cladding peak temperatures were obtained from the measured oxide layer thickness and by using measured temperatures as a basis for calculating oxide thickness from Equation (2). The measured temperatures are multiplied by a correction factor to obtain a corrected temperature profile, from which the calculated oxide thickness is compared with the measured value. This multiplication factor is changed incrementally, and the oxide thickness calculated for each change. The estimated cladding temperature is selected when the calculated oxide thickness is the same as the measured oxide thickness. This approach inherently assumes that the estimated temperatures are proportional to the measured temperature-time profiles.

For several isothermal temperatures, two to three samples were selected for different times at each temperature to compare the peak measured temperature with that calculated from Equation (2) using the temperature-time profiles and the measured reaction layer thickness for each sample. This analysis is handicapped, however, because the temperature history had to be manually digitized, and the estimated error reflects the random error from digitizing. Therefore, these estimates must be regarded as conservatively high.

Table 3 lists the measured and estimated temperature errors from the outside and inside surfaces. The experimentally measured values represent the total error in temperature and not only part, such as the error from oxide layer thicknesses from linear error propagation theory. The standard error (one standard deviation) in temperature from the outside surface is ± 35 K and from the inside surface is ± 30 K.

Linear error propagation theory was also used to estimate the accuracy of the oxidation method using the errors listed in Equation (2) and assuming errors of 5% in time and 10% in oxide thickness measurements. The maximum estimated error varies from 40 K at 973 K to 56 K at 1223 K

Table 3. Summary of temperature errors from isothermal samples

Sample Number	Temperature Outside (K)	Difference Inside
154	+25.0	+18.0
110	-0.80	-28.0
77	-9.50	-16.0
106	+13.6	-1.50
68	-4.90	+0.60
97	+1.60	-0.90
28	-57.30	-69.50
156	+26.80	+14.60
69	-3.50	-5.60
149	+60.8	+64.10
125	+16.2	+30.3
126	-18.1	+0.40
114	+26.1	-46.5
115	+38.0	+25.6
46	+31.1	-16.0
127	20.8	-21.60
61	+20.0	+27.0
Average	± 28.7	± 31.1

(see Appendix C). The contribution to the total error arises mainly from the errors in the constants in Equation (2). For example, 40% of the 40 K error can be attributed to the preexponential constant, and 57% to the error in activation energy. The error in time contributes the smallest error, about 0.2%; therefore, prior cladding peak temperatures may be estimated from fuel rods without measured thermal histories because gross errors in assumed time may be tolerated. However, to evaluate prior cladding peak temperatures of uninstrumented fuel rods in LOFT, temperature-time profiles were selected from symmetrically located, instrumented fuel rods.

Three samples that experienced double peak transients (Figure 10) were evaluated to determine the effect of double peak transients on the estimated peak cladding temperatures. The measured and estimated peak temperatures for the three samples are listed in Table 4. In this temperature range the difference in measured and estimated peak cladding temperatures is within the experimental error so that no transient effect can be concluded, in contrast with the transient effect observed between 1473 and 1673 K.

An electrical heater rod[34] and three nuclear fuel rods[17] that had been subjected to a series of LOCEs were used to evaluate the use of oxidation kinetics to determine prior cladding peak temperature in the $\alpha + \beta$ temperature region. The electrical heater rod was subjected to four LOCE transients during which a peak temperature of 1125 K was measured. The first nuclear rod was subjected to three LOCEs, and a peak temperature of
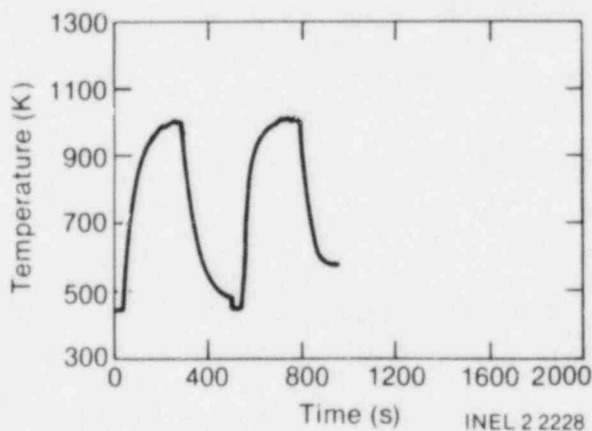
Table 4. Estimated prior peak temperatures for samples with multiple transients

| Sample | Peak Temperatures (K) | | Error (K) |
	Measured	Estimated	
132	952.7	1185.5	—
	1202.7	1185.5	+17.2
133	1005.7	—	—
	1112.0	1129.8	+17.8
134	1010.8	—	—
	1008.3	1096.7	88.4

1070 K was measured; the second nuclear rod was subjected to only one LOCE, during which a peak temperature of 1200 K was measured; and the third nuclear rod was subjected to four LOCEs, during which a peak temperature of 1125 K was measured.

Temperature estimates for the electrical heater rod from oxidation kinetics and the relative location of these temperature estimates are shown in Figure 11, with the cross section of the electrical heater rod taken at the junction of the thermocouples. Details of the microstructures and oxide layers for the different locations are shown in Figures 12 to 16. Based upon the oxidation kinetics, the peak cladding temperature was 1191 K and occurred opposite the two surface thermocouples. The temperatures near the two surface thermocouples were 1159 and 1145 K. For the different oxide thicknesses, the temperature varied from 1141 to 1191 K, resulting in a 50 K variation around the circumference of the zircaloy cladding. An estimated temperature of 1141 K at the thermocouple locations is slightly higher than the measured peak temperature of 1125 K. This difference suggests a small thermocouple effect on cladding temperature. This effect is further illustrated by the higher temperature measured between the thermocouples.

Temperature estimates from zircaloy microstructures are consistent with those from oxidation kinetics. Figures 12 and 13 show a redistribution of

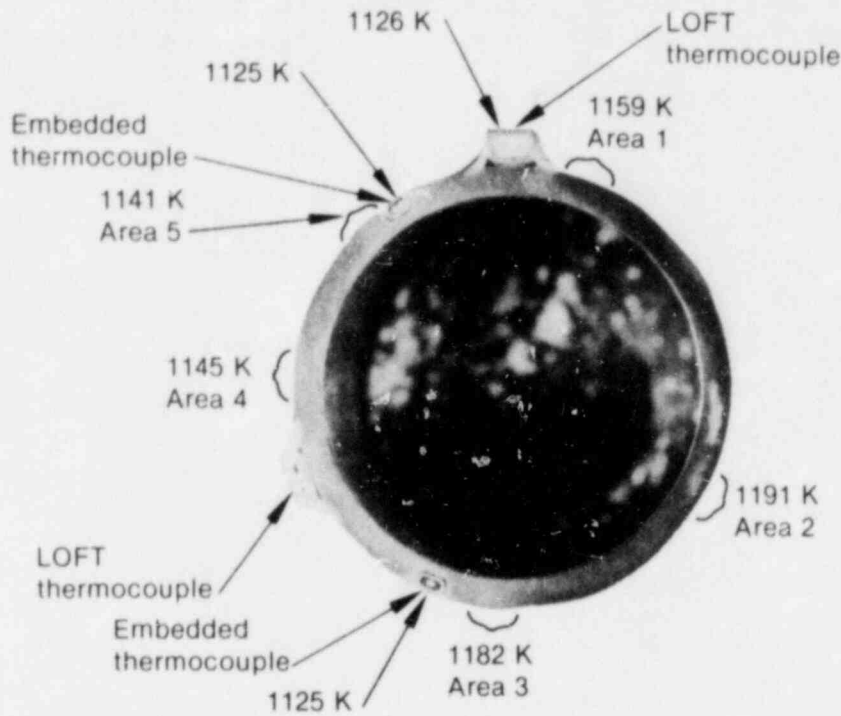Figure 10. Typical temperature-time history for multiple transients.

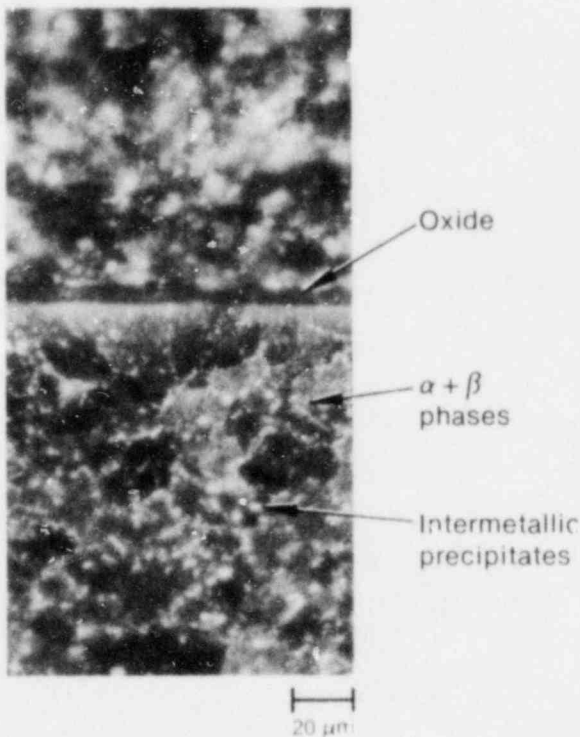Figure 11. Estimated cladding temperatures at thermocouple locations.

Figure 12. Oxide layer and zircaloy microstructure at Area 1.

the intermetallic precipitates from within the grains to the grain boundaries. This redistribution indicates that the cladding temperature had to exceed 1103 K, which is the $\alpha/\alpha + \beta$ transition temperature. From the amounts of precipitates in the grain boundaries (see Appendix C), the temperature shown in Figure 16 for Area 5 is less than that in Area 1 (Figure 12), and both temperatures are less that that in Area 2 (Figure 13). These results are consistent with the temperatures derived from oxidation kinetics.

The temperature estimates for the nuclear fuel rods were 1076 K compared with 1070 K measured for the first rod, 1186 K compared with 1200 K measured for the second rod, and 1145 K compared with 1125 K measured for the third rod. Calculated temperatures for two of the three rods were higher than the measured temperatures, which would be expected from thermocouple effects on cladding temperature. The low estimated temperatures for the second nuclear rod may be due to sloughed oxide or the lack of any thermocouple effect.
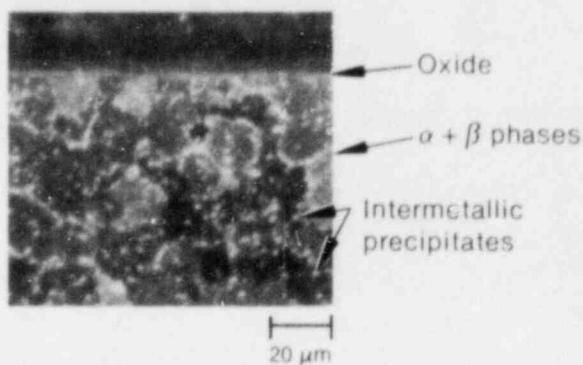
14

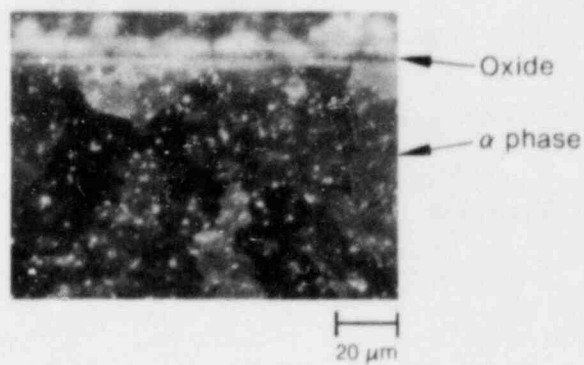Figure 13. Oxide layer and zircaloy microstructure at Area 2.

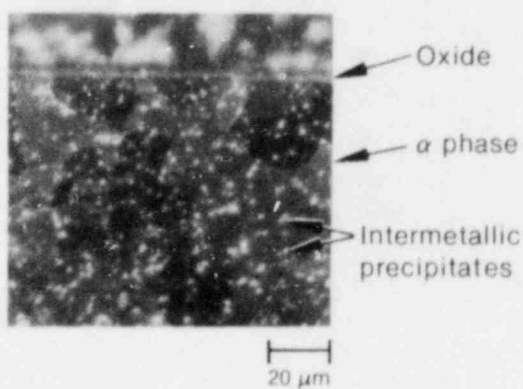Figure 15. Oxide layer and zircaloy microstructure at Area 4.

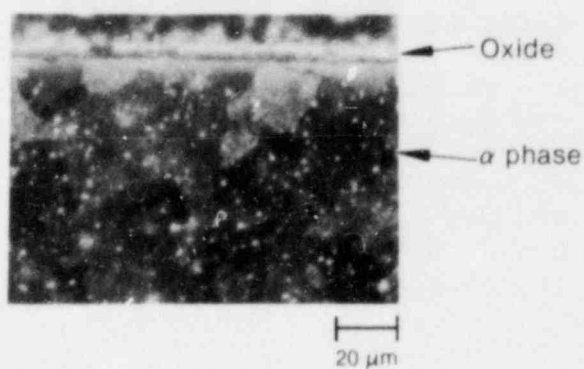Figure 14. Oxide layer and zircaloy microstructure at Area 3.

Figure 16. Oxide layer and zircaloy microstructure at Area 5.

Temperature measurements were evaluated from three nuclear fuel rods subjected to PCM conditions, in which the coolant flow is reduced while the power generation in the fuel rods is still high.[4] The temperature differences between the measured and estimated temperatures were 526, 255, and 613 K. These differences are considerably higher than those for rods tested under LOCE conditions with much lower power generation. The larger PCM differences are attributed to the "fin effect" of the surface thermocouple conducting the heat flux from the fuel rod.

The reasonably good agreement between estimated and measured temperatures shows that oxidation kinetics is a viable technique for estimating cladding temperature. Because the cladding temperature for this electrical heater rod exceeded the α to $\alpha + \beta$ transformation at several azimuthal locations, zircaloy microstructures were used effectively to complement the temperature estimates from oxide thickness measurements. The microstructures confirmed the circumferential temperature variation determined from oxidation kinetics.

CONCLUSIONS

Metallurgical examinations of zircaloy cladding during PIE offer two independent techniques for estimating cladding temperatures. The first technique, based upon zircaloy microstructure, permits determination of temperature range through identification of allotropic phases and knowledge of the transition temperatures. This technique can be improved by using the fraction of transformed α phase (prior α) in the two-phase $\alpha + \beta$ phase region and the temperature range of the two-phase region. The latter method can provide accurate temperature estimates without relying on time-at-temperature relationships, but the technique depends upon a human element of interpretation of the β fractions with poor resolution of the α and transformed β phases. The second technique matches a measured oxide thickness from PIE with a calculated value from the oxidation kinetics and a temperature-time profile. This technique can provide precise temperature estimates, although the temperature-time profile is required.

Because the time error contribution is small, relatively large time errors can be tolerated.

The oxidation kinetic data obtained at INEL in the two-phase $\alpha + \beta$ region extend the knowledge of oxidation kinetics in this region. Parabolic kinetics were confirmed in this temperature region and at atmospheric pressure, and the data are validated by comparison with other oxygen uptake data in the literature.

The INEL oxidation kinetic equations have been applied to one electrical heater rod subjected to four LOCEs and three nuclear fuel rods each subjected to one to three LOCEs. The estimated peak temperatures compared favorably with the measured temperatures within ± 20 to 30 K. This comparison demonstrates that the parabolic oxidation kinetics in the two-phase temperature region can be applied to LOCEs to estimate prior peak cladding temperatures and that high pressure effects are negligible during LOCEs.

REFERENCES

1. *Acceptance Criteria for Emergency Core Cooling Systems for Light Water Cooled Nuclear Power Reactors*, Docket No. RM-50-1, Nuclear Regulatory Commission, December 28, 1973.

2. R. G. Ballinger, W. G. Dobson, and R. R. Biederman, "Oxidation Reaction Kinetics of Zircaloy-4 in Unlimited Steam Environment," *Journal Nuclear Materials 62*, 1976, pp. 213-220.

3. S. L. Seiffert and G. R. Smolik, *Post Irradiation Examination Results for the Power-Cooling-Mismatch Test 2A*, TREE-NUREG-1029, February 1977.

4. S. L. Seiffert, *Power-Coolant-Mismatch Test Series PCM-2 Post Irradiation Examination*, TREE-NUREG-1069, March 1977.

5. S. Ploger et al., *Post Irradiation Examination Results for the Irradiation Effects Test 2*, TREE-NUREG-1195, January 1978.

6. D. W. Croucher et al., *Irradiation Effects Test Series, Test IE-5 Test Results Report*, TREE-NUREG-1130, January 1978.

7. S. Ploger et al., *Post Irradiation Examination Results for the Irradiation Effects Test IE-3*, TREE-NUREG-1299, March 1978.

8. T. F. Cook et al., *Post Irradiation Examination Results for the Irradiation Effects Test IE-5*, TREE-NUREG-1201, March 1978.

9. E. Gebhardt et al., "Untersuchungen in System Zirkonium-Sauerstoff, Teil 2: Untersuchungen zur Kinetic der Reaction Zwischen Zirkonium und Sauerstoff, sowie uber die Konstition des Systems Zirkonium-Sauerstoff," *Journal Nuclear Materials 4*, 1961, p. 255.

10. R. L. Beck, "Zirconium-Hydrogen Phase System," *Trans. ASM 55*, 1962, p. 542.

11. M. L. Picklesimer, "Method of Annealing and Rolling Zirconium Base Alloy," U.S. Patent 2,894,866, July 14, 1959.

12. C. S. Olsen, *Effects of Irradiation Upon Zircaloy Microstructures and Transformation Temperatures*, RE-M-77-010, EG&G Idaho, Inc., September 30, 1977.

13. H. M. Chung et al., "Mechanical Properties of Zircaloy Containing Oxygen," *Light-Water-Reactor-Safety Research Program Quarterly Progress Report, January-March 1976*, ANL-76-49, 1976, p. 37.

14. W. M. Rumball, *The Hardenability of Zr-1.2 wt% Cr-0.1 wt% Fe*, AECL 3050, 1968.

15. J. V. Cathcart et al., *Zirconium Metal-Water Oxidation Kinetics, Part 4: Reaction Rate Studies*, ORNL-NUREG-17, August 1977.

16. J. M. Broughton et al., *PBF-LOCA Test Series, Test LOC-11C Experiment Test Prediction*, TFBP-TR-259, February 1978.

17. D. J. Varacalle, Jr. et al., *PBF/LOFT Lead Rod Test Series Test Results Report*, NUREG/CR-1538, EGG-2047, July 1980.

18. J. J. Kearns et al., "Effect of Alpha/Beta Phase Constituent on Superplasticity and Strength of Zircaloy-4," *Journal Nuclear Materials 61*, 1976, pp. 169-184.

19. J. C. Greenbank and S. Harper, "Solute Distribution in Oxidized Zirconium Alloys," *Electrochemical Technology 4*, 1966, p. 142.

20. B. Nath et al., "Effect of Hydrogen Concentration and Cooling Rate on Hydride Precipitation in α-Zirconium," *Journal Nuclear Materials 58*, 1975, pp. 153-162.

21. R. Biederman et al., *A Study of Zircaloy-4-Steam Oxidation Reaction Kinetics*, EPRI NP-225 (PB 260 693), September 1976.

22. L. Baker Jr. and L. C. Just, *Studies of Metal-Water Reactions at High Temperatures Part III: Experimental and Theoretical Studies of the Zirconium-Water Reactions*, ANL-6548, May 1962.

23. W. A. Bostrom, *The High Temperature Oxidation of Zircaloy in Water*, WAPD-104, March 19, 1954.

24. A. W. Lemmon Jr., *Studies Relating to the Reaction Between Zirconium and Water at High Temperature*, BMI-1154, January 8, 1957.

25. J. P. Pemsler, "Studies on the Oxygen Gradients in Oxidizing Metals," *Journal Electrochemical Society 112*, 1965, p. 477.

26. C. J. Rosa and W. W. Smeltzer, "The Parabolic Oxidation Kinetics of Beta-Zirconium," *Acta Metallurgica 13*, 1955, p. 55.

27. R. E. Pawel et al., *Zirconium Metal-Water Oxidation Kinetics, Part V: Oxidation of Zircaloy in High Pressure Steam*, ORNL-NUREG-31, December 1977.

28. R. J. Hussey and W. W. Smeltzer, "The Mechanism of Oxidation of Zirconium in the Temperature Range 400-850°C," *Journal Electrochemical Society 111*, 1964, p. 1221.

29. G. R. Wallwork et al., "The Parabolic Oxidation Kinetics of Alpha Zirconium at 850°C," *Acta Metallurgica 12*, 1964, p. 409.

30. M. Leclercq, *Contribution a L'Etude du Mecanism D'Oxydation du Zirconium Pur ou Allie par L'Oxygene et La Vapeur D'Eau*, EUR 4507, 1970.

31. S. Malang, *SIMTRAN I—A Computer Code for the Simultaneous Calculation of Oxygen Distributions and Temperature Profiles in Zircaloy During Exposure to High-Temperature Oxidizing Environments*, ORNL-5083, November 1975.

32. Z. R. Martinson, *Behavior of 5-Inch-Long, 1/4-Inch-OD, Zircaloy-2 Clad Oxide Fuel Rods Subjected to High Energy Power Bursts*, IN-ITR-107, August 1969.

33. S. Leistikow et al., *Kinetic und Morphologie der Isotherman Dampf-Oxidation von Zircaloy 4 bei 700-1300°C*, KFK 2587, March 1978.

34. C. S. Olsen, *Posttest Examination of Electrical Heater Rods Tested in the Blowdown Facility*, LTR LO-00-80-116, May 15, 1980.

APPENDIX A
ZIRCALOY MICROSTRUCTURES

APPENDIX A
ZIRCALOY MICROSTRUCTURES

The role of zircaloy microstructures in estimating temperatures is addressed in this section, important parameters are identified and the current data base is discussed. Transition temperatures and the use of microstructures to deduce the transition temperatures are described below, followed by a discussion of zircaloy microstructures for phase identification, including a method for finer resolution of temperatures in the $\alpha + \beta$ temperature region; finally, the discrepancies in the data base are summarized.

Transition Temperatures for α/β Transformation

Zircaloy microstructures have been used to estimate peak cladding temperatures from the presence of alpha (α) or beta (β) phases during thermal transients.[A-1] The alloying elements tin, iron, chromium, and in zircaloy-2, nickel, expand the instantaneous (diffusionless) α/β transformation in pure zirconium from a single temperature (1135 K) to a temperature range (1103 to 1243 K). These solutes, normally considered to be in solid solution, precipitate during temperature excursions. The formation of three phase regions (α, $\alpha + \beta$, and β) and the distribution of the precipitates form a basis to identify cladding temperatures from zircaloy microstructures. Also, the microstructure change from cold-worked to annealed cladding can be used to identify a cladding temperature in the high α phase region.

The temperature estimates are derived from the transition temperatures of the zircaloy phase changes,[A-2] once the phases are identified from the zircaloy microstructures. The α to $\alpha + \beta$ transition establishes a temperature of 1103 K[A-2] and the $\alpha + \beta$ to β transition establishes a temperature of 1243 K.[A-2] For a particular location on the cladding, if the microstructure is identified as β phase, the cladding temperature would be >1243 K; if the $\alpha + \beta$ phase were identified, the cladding temperature would be between 1103 and 1243 K. If only the α phase is present, cladding temperature would be <1103 K. An instantaneous annealing temperature of 866 K occurring in the high α region but below the α to $\alpha + \beta$ transition is another point that can bracket a temperature range in the high α phase region.[A-3]

These transition temperatures are based upon the normal alloy content of zircaloy-2 or -4 (1.5% Sn, 0.1% Cr, 0.2% Fe with Fe + Cr = 0.28%). During LOCE conditions, hydrogen and oxygen may dissolve into the cladding. Oxygen is an α stabilizer and raises the $\alpha/\alpha + \beta$ transition temperatures.[A-4] On the other hand, hydrogen is a β stabilizer and lowers the $\alpha + \beta/\beta$ transition temperatures.[A-5] If both are simultaneously dissolved and do not interreact with each other, their separate effects will not be compensated. In the β phase, the presence of oxygen reduces the solubility of hydrogen, but data are not available on the effect of oxygen upon hydrogen solubility in the α phase.[A-6] Oxygen and hydrogen contents in conjunction with phase equilibria must be taken into account to assess the transformation temperatures.[A-4,A-5]

Zircaloy Microstructures

To estimate cladding temperature ranges from microstructures, a correlation between microstructure and the α, $\alpha + \beta$, and β phases is required under LOCE-type conditions. Microstructures obtained under other types of conditions may be different, and consequently incorrect interpretation of the microstructures may arise.

Zircaloy microstructures are characterized by grain size and shape, chemical composition, size and distribution of alloying precipitates, and the chemical composition and distribution of reaction products formed from chemical reaction of zircaloy and surrounding materials. These characteristics will be used to identify the phases and hence the temperature changes.

Microstructures obtained from conditions similar to those during a LOCE for the change from cold-worked to annealed cladding and recrystallization for the three phase fields, α, $\alpha + \beta$, and β will be presented next. These microstructures typify the catalogue of microstructures presently available.

Change from Cold-Worked to Recrystallized Zircaloy. Because of the rapid heat-up during a LOCE, an instantaneous annealing temperature for a complete change from cold-worked to

annealed cladding can be used to estimate cladding temperature rather than the traditional recrystallization temperature based upon 50% recrystallization in 1 h, for example. The recrystallization of cold-worked LOFT cladding and an instantaneous recrystallization temperature were determined from both hardness measurements and zircaloy microstructures.[A-3]

Zircaloy samples were heated from 589 K at about 110 K/s to the desired temperature, held at temperature for a specified time, and rapidly cooled to room temperature. Samples were also heated for three successive transients similar to the single-cycle transient, but with the samples reheated after the first two cycles when the temperature dropped below 589 K. The total time at temperature for a particular triple-cycle specimen was equal to the total time at temperature for a corresponding single-cycle specimen.

Hardness measurements performed with a diamond-pyramid indenter with a 1-kg load and metallography were used to determine the annealing temperature. Initially, four midwall readings were taken from each ring, with the impressions spaced every 90 degree from the thermocouple attachment position. The short-duration tests produced specimens with varying hardness in the circumferential direction due to uneven heating rates that created temperature differences around the specimen. Hardness readings for these specimens were repeated and concentrated near the thermocouple position—the position of maximum confidence in temperature.

The results of the hardness measurements demonstrate that significant annealing of the zircaloy tubes can occur in relatively short times at temperatures of 922 K and above. Figure A-1 shows the hardness results as a function of maximum nominal test temperature. The average hardness of the as-received material was 237 Diamond Pyramid Hardness (DPH). All tests conducted at a maximum temperature of 811 K produced average sample hardness only slightly less than the as-received material (230 to 235 DPH). The 866 K test samples clearly showed typical annealing behavior with the shorter test times producing little hardness drop (230 to 237 DPH) and the longer times producing almost fully softened material (182 to 192 DPH). Samples cycled to maximum temperatures of 977 and 1033 K were completely softened even after the minimum test times.
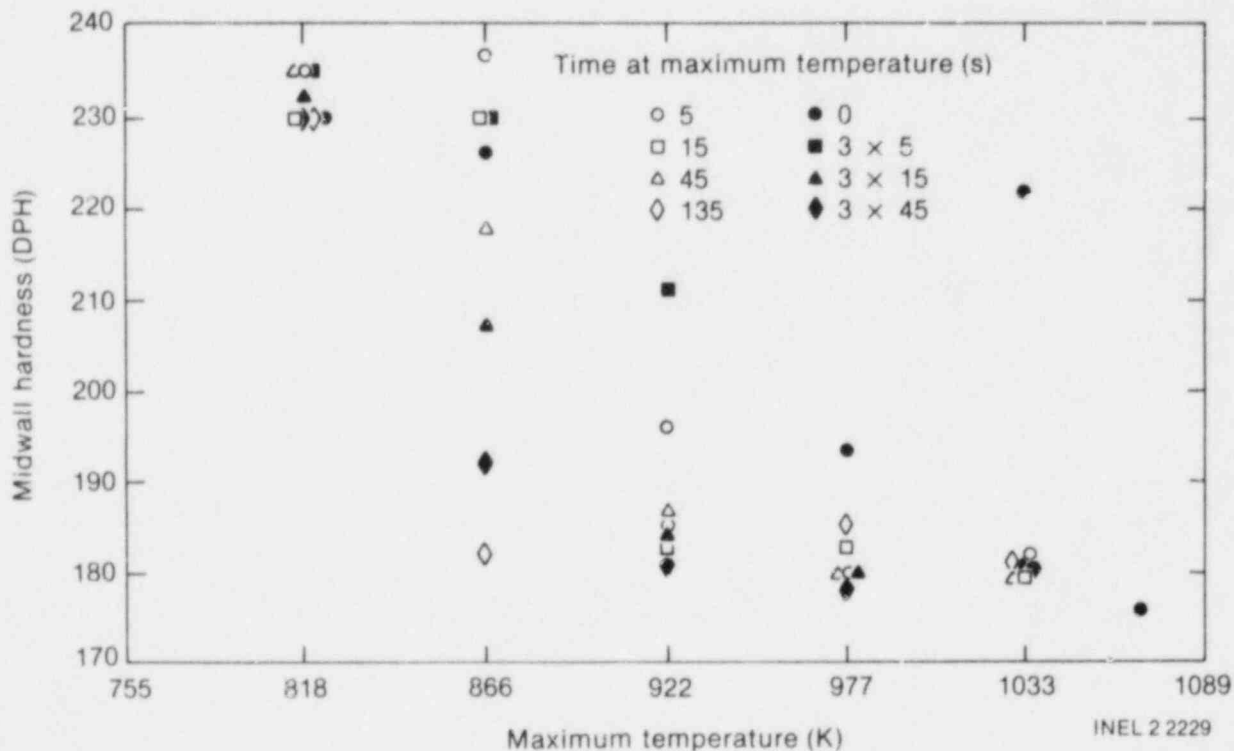

Figure A-1.   Hardness results for all transient tests.

As shown in Figure A-1, the annealing behavior of LOFT cladding subjected to a triple transient at any particular maximum temperature does not correlate with the corresponding single transient of similar duration. This behavior probably resulted from the very rapid heatup and cooldown rates employed in these tests. If slower rates had been used, the integrated time-temperature effect would probably have been more pronounced, and a triple-cycle transient would have resulted in lower hardness than the equivalent single cycle.

LOFT zircaloy tubing microstructures at different temperature and time exposures are shown in Figures A-2 to A-5. Figure A-2 is typical of the as-received cladding, and Figure A-3 shows the microstructure after heating at 811 K for 135 s. Both microstructures are characteristic of the cold-worked zircaloy with no distinct development of the gain structure.

Figures A-4 and A-5 show the microstructures of samples heated at 866 K for 5 and 15 s, respectively. At 5 s, the structure is partially annealed. Some fine, equiaxed, recrystallized grains have formed, but some are still unresolved and give a blurry appearance to the structure. In contrast,

Figure A-5 indicates a completely recrystallized structure with all the grains clearly developed after a 15-s temperature exposure. At 922 K and for times of 5 and 15 s, microstructures similar to those in Figures A-4 and A-5, respectively, were obtained, thus recrystallization starts at 866 K rather than 922 K as derived from hardness measurements. This temperature may be reduced by annealing times longer than 15 s, but even at 135 s (the longest time used) at 811 K, no recrystallization took place. For expected LOCE times-at-temperature, 866 K is an appropriate value for the recrystallization temperature.

α **Phase Microstructure.** Figure A-5 shows the microstructure of a completely recrystallized α phase heated at 866 K and rapidly cooled. Only a few precipitates are visible. Upon heating to a higher temperature (1072 K for 300 s) in the α phase region (Figure A-6),[A-7] the grain structure remains essentially the same except that the number of precipitates is substantially increased, probably because of the slower cooling rate (<2 K/s) rather than the higher temperature. The microstructure shown in Figure A-5 was obtained after rapid cooling at an unspecified rate from 866 K.[A-3] Because of the higher temperature and
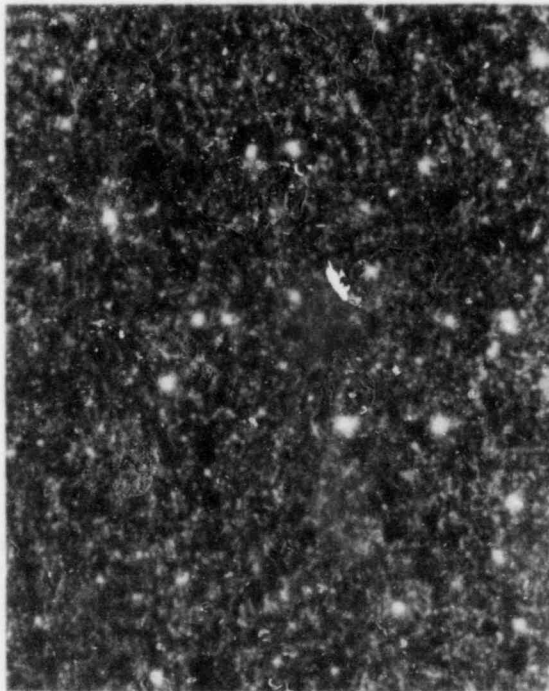

Figure A-2.   Microstructure of as-received, uncrystallized zircaloy.

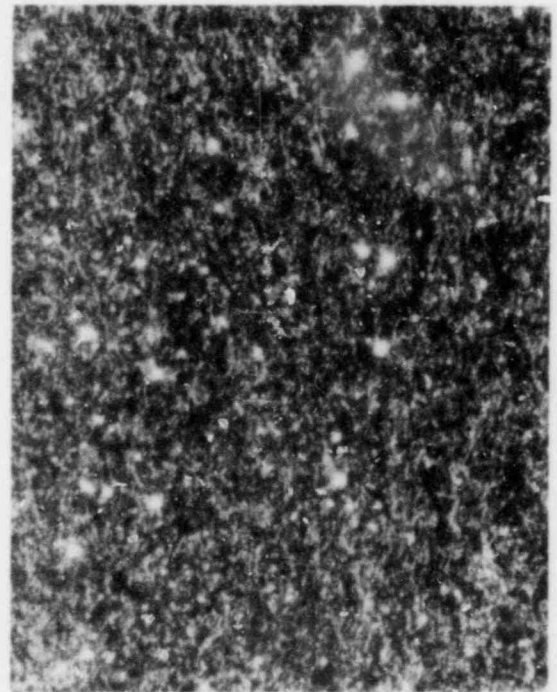Figure A-3.   Microstructure of unrecrystallized zircaloy after heating at 811 K for 135 s.
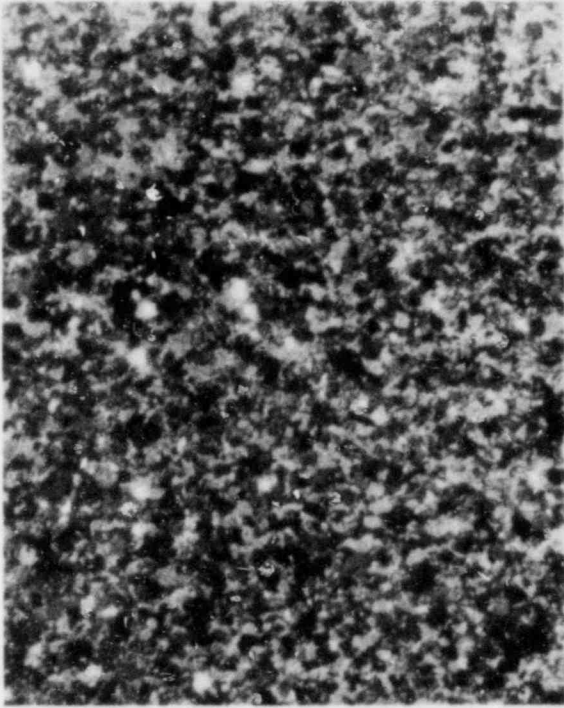
23

Figure A-4.   Microstructure of partially recrystal-lized zircaloy after heating at 866 K for 5 s.
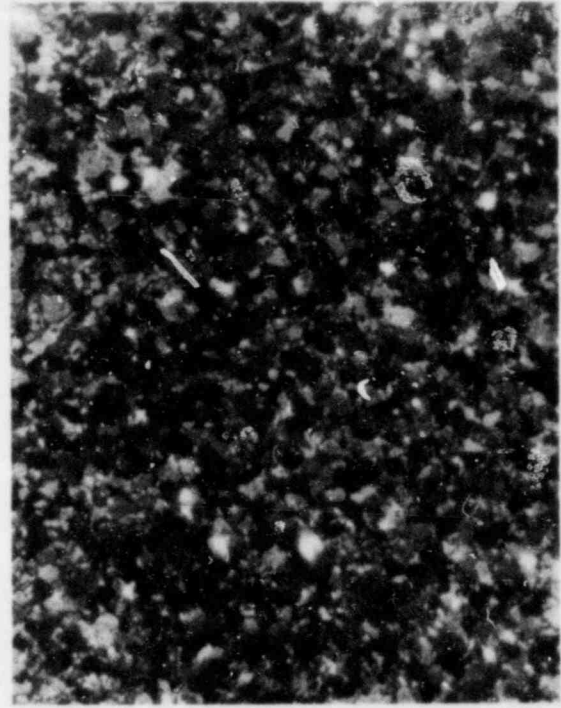
Figure A-5.   Microstructure of recrystallized zir-caloy after heating at 866 K for 15 s.
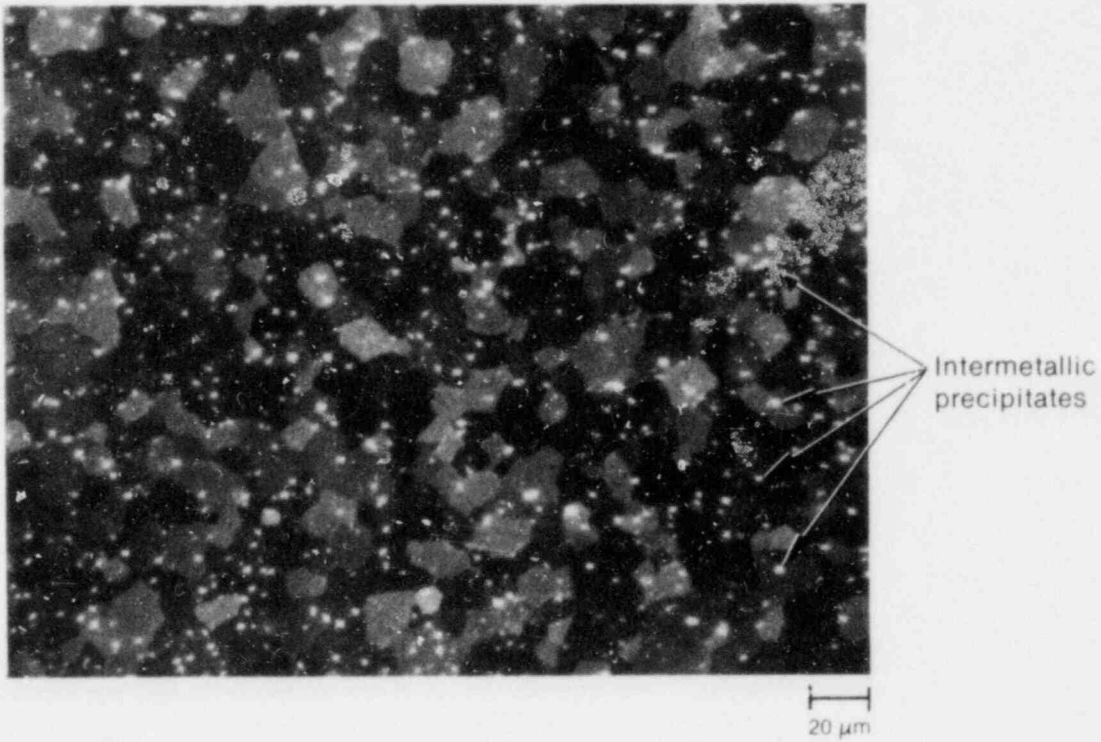

Intermetallic precipitates

20 μm

Figure A-6.   Microstructure of α phase (1070 K) with random precipitates.

longer heating time, the grain size shown in Figure A-6 is larger than that shown in Figure A-5. Grain growth is expected to start at 1020 K.

Figure A-7 shows the microstructure of irradiated zircaloy cladding after being heated to 1072 K and cooled at <2 K/s in vacuum. In addition to the intermetallic precipitates, hydrides are also found within the grains. Hydrides may not always precipitate within the grains, but may extend through several grains or be distributed on the grain boundaries.[A-8] The morphology of hydride precipitation has been shown to be affected by cooling rate.[A-8]

The hydrides shown in Figure A-7 formed as a result of a two- to three-year irradiation exposure at operating temperature in the Saxton reactor.[A-9]

Hydrogen pickup from zircaloy/steam reaction could be substantial for the temperatures expected for a LOCE. The hydride may form underneath an oxygen-rich α-zircaloy layer as depicted in

Figure A-8.[A-10] The outer layer consists of coarse, equiaxed, α-zircaloy grains with an inner layer of α-zircaloy grains with copious amounts of the acicular precipitate of zirconium hydride. The cooling rate, and to a lesser extent, the hydrogen content affects the morphology of the hydrides in zirconium.[A-11,A-12] In the α phase temperature
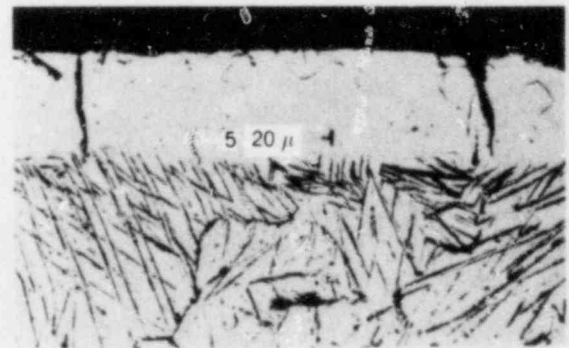

Figure A-8. Microstructure of cracked oxygen-rich layer and underlying hydride needles after heating in steam at 948 K for 360 h.
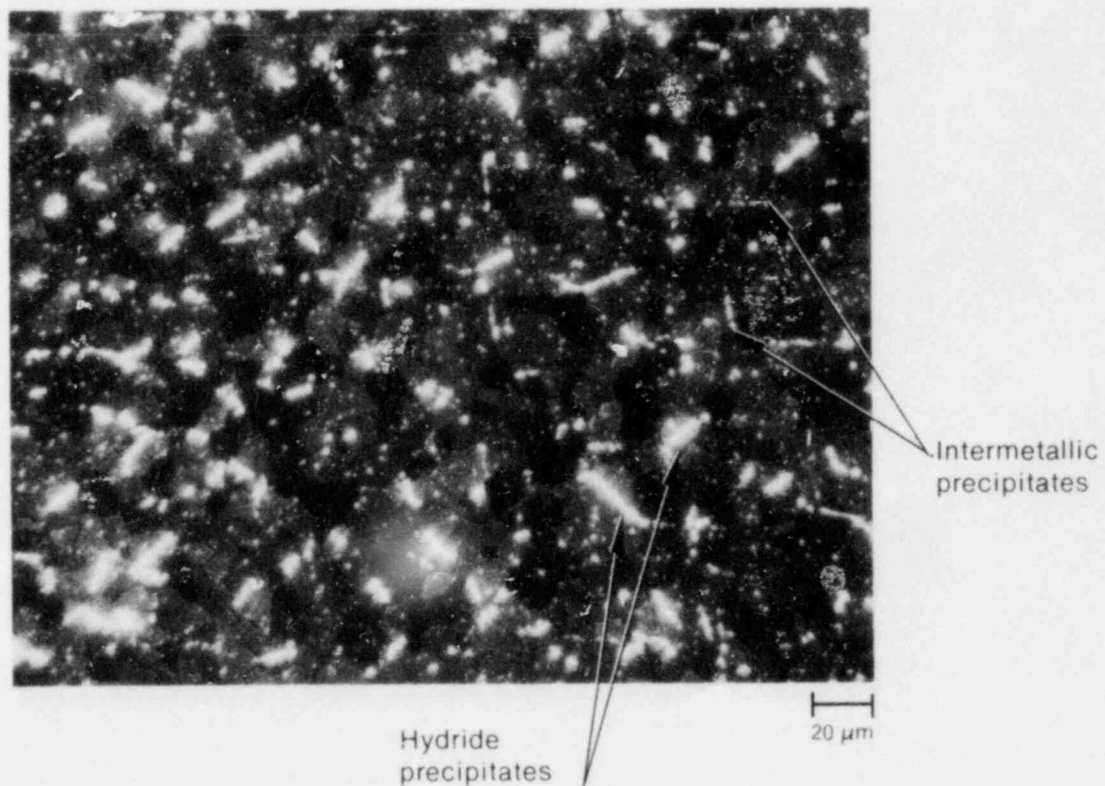

Figure A-7. Microstructure of irradiated zircaloy heated at 1072 K for 300 s and cooled at ~1 K/s.

25

region, the propensity of hydride precipitation is intragranular in the form of σ hydrides (face-centered tetragonal) at high cooling rates (10,000 to 20,000 K/s). As the cooling rate decreases the hydrides precipitate in the grain boundaries in the form of δ hydrides (face-centered cubic). For a given cooling rate, and increasing the hydrogen content, δ hydrides tend to precipitate in both intra- and intergranular sites. The hydride morphology is summarized in Table A-1. The hydride precipitation shown in Figure A-8 apparently occurred under rapid cooling conditions.

$\alpha + \beta$ **Phase Microstructures**. The zircaloy microstructures in Figure A-9 show different proportions of β phase in the two-phase $\alpha + \beta$ region.[A-13] These microstructures were obtained from zircaloy samples loaded with 700 to 2700 ppm hydrogen and heated in an inert atmosphere so that different proportions of prior β phase are formed by quenching from 1005 K. In Figure A-9, β phase forms at the α grain boundaries and isolates the α grains from other α grains as the proportion of β phase increases. Although hydrogen was introduced only to vary the proportions of the β phase, the hydride has still left its mark on the microstructure through the appearance of platelets within the grains. Also, the β grains in a two-phase $\alpha + \beta$ region may resemble the microstructure shown in Figure A-9c for 100% β phase with rapid rates of cooling. This microstructure is not apparent in Figures A-9a and b, possibly because of the hydride introduced into the samples.

Figures A-10 and A-11 show two $\alpha + \beta$ microstructures, one unirradiated and heated in vacuum to 1115 K and the other irradiated and heated in vacuum to 1234 K.[A-7] Both microstructures resulted from slow cooling (< 2 K/s), and are distinctly different from those depicted in Figure A-8. In Figure A-10, the equiaxed grain shape is not significantly different from the α structure (Figures A-5 to A-7), but the intermetallic precipitates were redistributed from within the grains to the grain boundaries.

These precipitates are an intermetallic compound of zirconium, iron, and chromium (Figure A-12). The zirconium is preferentially etched around these precipitates, leaving the precipitates on the surface to reflect the light and thus appearing as white spots in polarized light. These precipitates may be removed by swabbing the surface.

Upon cooling at rates >6 to 10 K/s, the precipitates do not appear in either the grain boundaries or in the grains (Figure A-13). The faster cooling rates may completely inhibit the nucleation and growth of these precipitates or the precipitates may be so fine as to be unresolvable with the light microscope.

With irradiated cladding shown in Figure A-11, the additional hydride precipitates are still associated within the grains, rather than at the grain boundaries with the intermetallic precipita... nuclear testing[A-6] indicate

Table A-1. Summary of results of metal examination to study the effect of rate of cooling and/or the hydrogen content of alloys on the precipitation behavior of the hydrides

Hydrogen Content (ppm)	Water-Quench (~10,000 K/s)	Oil-Quench (~1,000 K/s)	Air-cool (2 to 10 K/s)	Furnace-cool (<2 K/s)
50	Intragranular γ-hydride needles in three (1120) directions.	Intragranular γ-hydride plates in three (1120) directions.	Intragranular γ-hydrides in three (1120) directions. Intragranular σ-hydrides. Intergranular γ-hydrides.	Even distribution of heterogeneously nucleated δ-hydrides, mainly at the grain boundaries.
200	Intragranular γ-hydrides in three (1120) directions. Alignment into bands.	Intra- and intergranular γ-hydrides. Alignment into stringers.	γ and δ-hydrides at intra- and intergranular sites. Irregular interface with the matrix.	Grouping of heterogeneously nucleated δ-hydrides mainly at the grain boundaries.
500	γ and δ-hydrides at intra- and intergranular sites. Alignment into bands and stringers.	δ-hydrides at intra- and intergranular sites. Irregular interfaces with the matrix.	δ-hydrides mainly at the grain boundaries. Irregular interfaces with the matrix.	Groups of heterogeneously nucleated δ-hydrides mainly at the grain boundaries.
640	δ-hydrides at intra- and intergranular sites. Alignment into bands.	δ-hydrides at intra- and intergranular sites. Irregular interfaces with the matrix.	Colonies of intra- and intergranular δ-hydrides. Irregular interfaces with the matrix.	Equiaxed hydrides. Few intragranular hydrides.
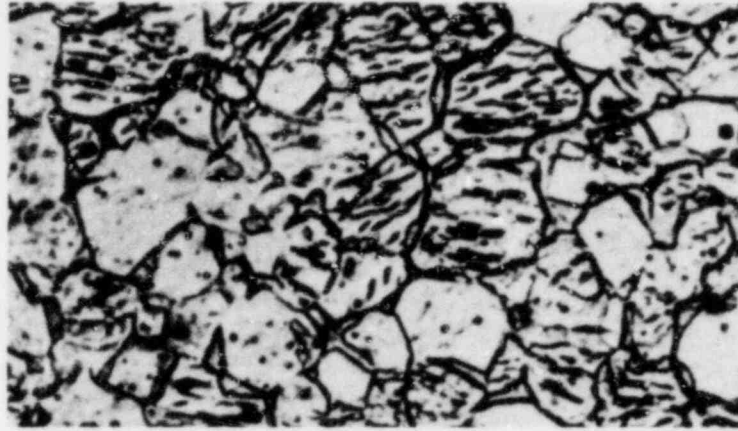
(a) 700 ppm H 12% β

(b) 1100 ppm H 47% β

(c) 2700 ppm H 100% β

Figure A-9.   Microstructures of the two-phase, $\alpha + \beta$, region for different proportions of β after heating for 1-1/2 h at 805 K.

Intermetallic
precipitates

Figure A-10.   Microstructure of irradiated Zircaloy heated at 1115 K ($\alpha + \beta$) for 300 s and slowly cooled.
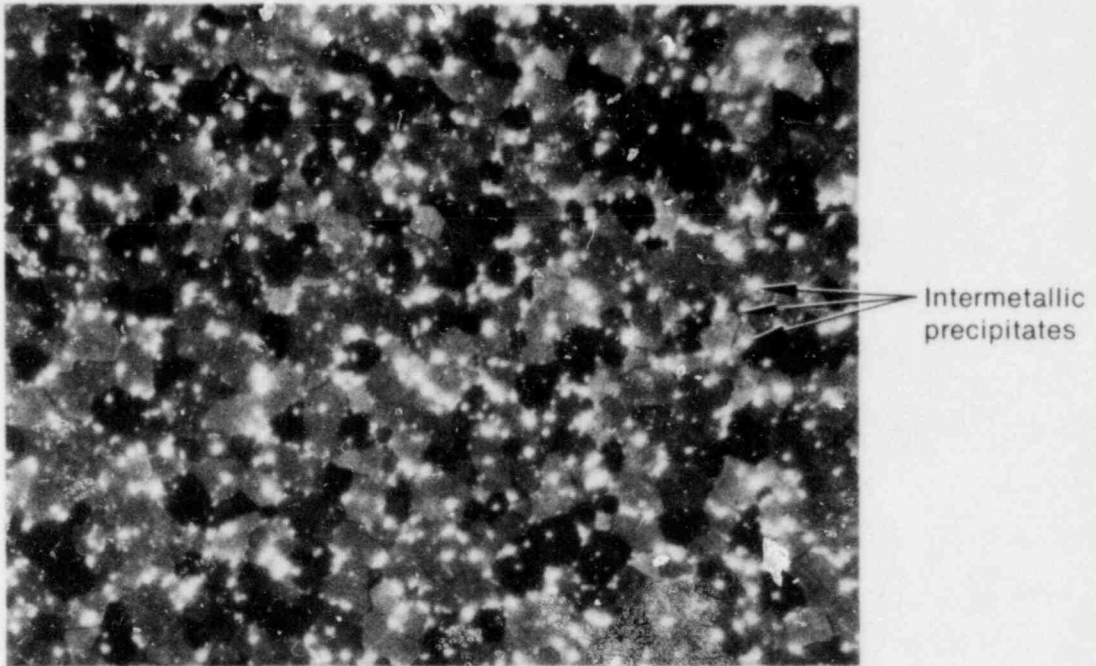

Hydride
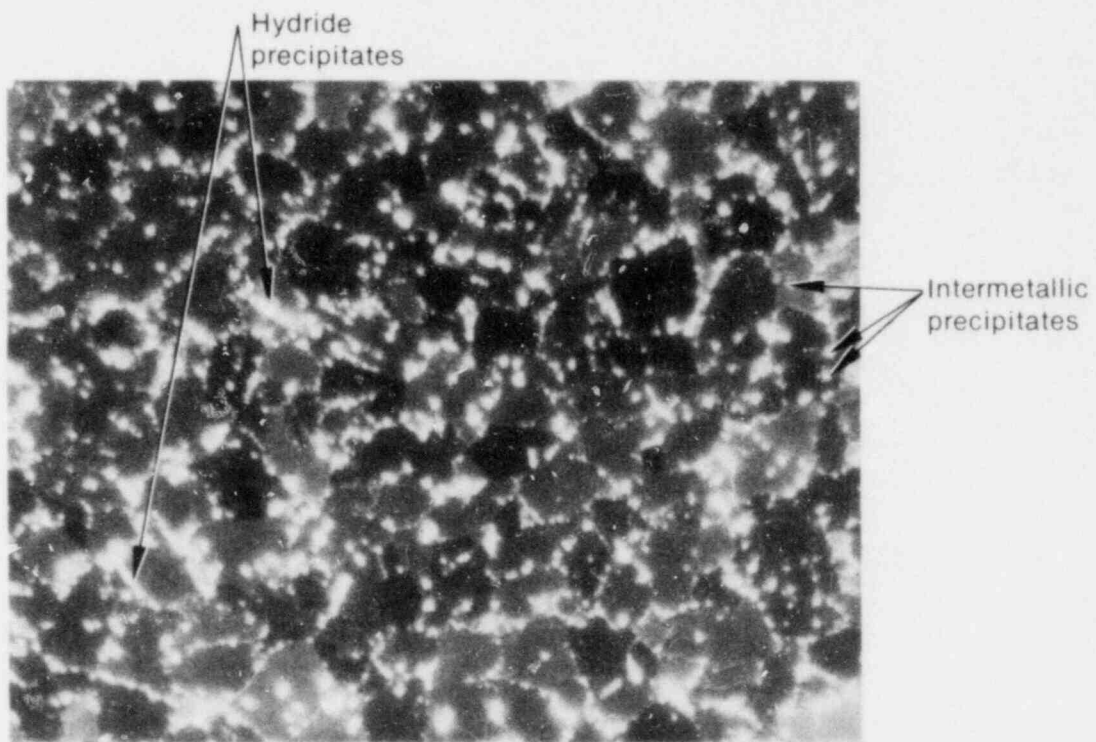precipitates

Intermetallic
precipitates

Figure A-11.   Microstructure of irradiated Zircaloy heated at 1234 K ($\alpha + \beta$) for 300 s and slowly cooled.
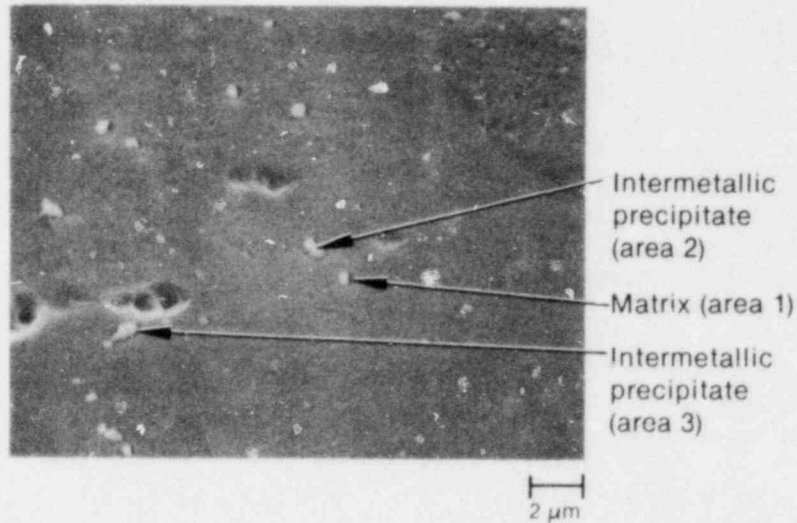
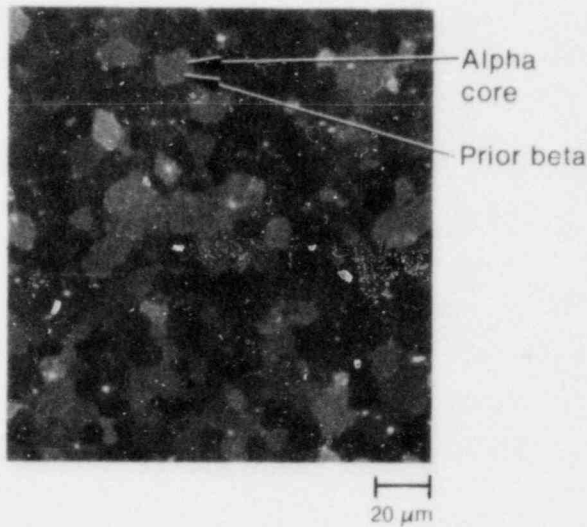Figure A-12.   Intermetallic precipitates in the α phase.

Figure A-13.   α + β microstructure heated at 1147 K and cooled at ~10 K/s with no precipitation.
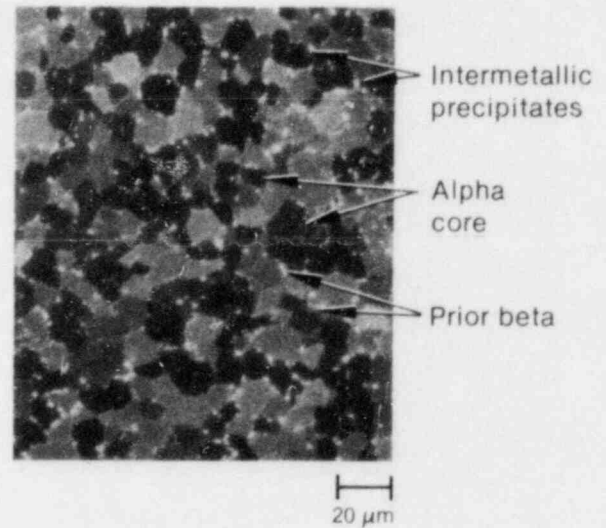
Figure A-14.   α + β microstructure heated at 1161 K and cooled at ~1 K/s.

that hydrides are precipitated within the grain boundaries. This effect may be attributed to differences in cooling rates.

The microstructure of zircaloy in the two-phase region exhibits slightly different characteristics in bright field (Figure A-14). The α phase appears as a core in the center of the grain surrounded by the transformed β structure which appears as a little lighter field than the α core.

Upon heating zircaloy samples to temperatures in the two-phase α + β region in air, the zircaloy

microstructure progressively changed for several minutes. This transition was determined to be a retardation of the α to α + β transformation. This time effect is not consistent with the instantaneous transformation in pure zirconium, but was speculated to arise from the slow rate of segregation of alloying elements at the grain boundaries which normally enhances the transformation. Microstructures obtained from samples heated in a vacuum exhibited microstructure different from that obtained in air, indicating that if the time effect were real, the presence of oxygen would be important in distinguishing the progress

29

of the α to $\alpha + \beta$ transformation with time. However, oxidation tests in the intermediate temperature range have not confirmed this retardation in the α to $\alpha + \beta$ transformation so the results apparently reflect the role of the environment upon the zircaloy microstructure. Zircaloy microstructures are very sensitive to cooling rate in the two-phase, $\alpha + \beta$ region. This effect may also be a factor in the anomalous time effect.

The temperature range of the α/β transformation and estimates of the fraction of the α phase were used to estimate prior cladding peak temperatures. The α phase in the two-phase field is characterized by a very light gray in a white matrix in bright field (Figure A-14). The fraction of α is estimated in grains selected with this structure. The temperature estimate is than obtained from:

$$T_{est} = 1103 + X_\alpha (1243 - 1103) \qquad (A-1)$$

where

$T_{est} =$ estimated temperature

$X_\alpha =$ fraction of α phase.

This technique was used to estimate cladding temperatures of about 20 samples for which measured temperatures were not previously known. With minimization of any bias from prior knowledge, the cladding temperatures were estimated within ± 20 K of the measured temperatures (Figure A-15).

Using bright field light with etched samples, resolution of the α phase is not clear. This poor resolution results in heavy emphasis on personal judgment to delineate the α phase and the amount of the α phase. Because of this judgmental factor, considerable variation may result from technician to technician.
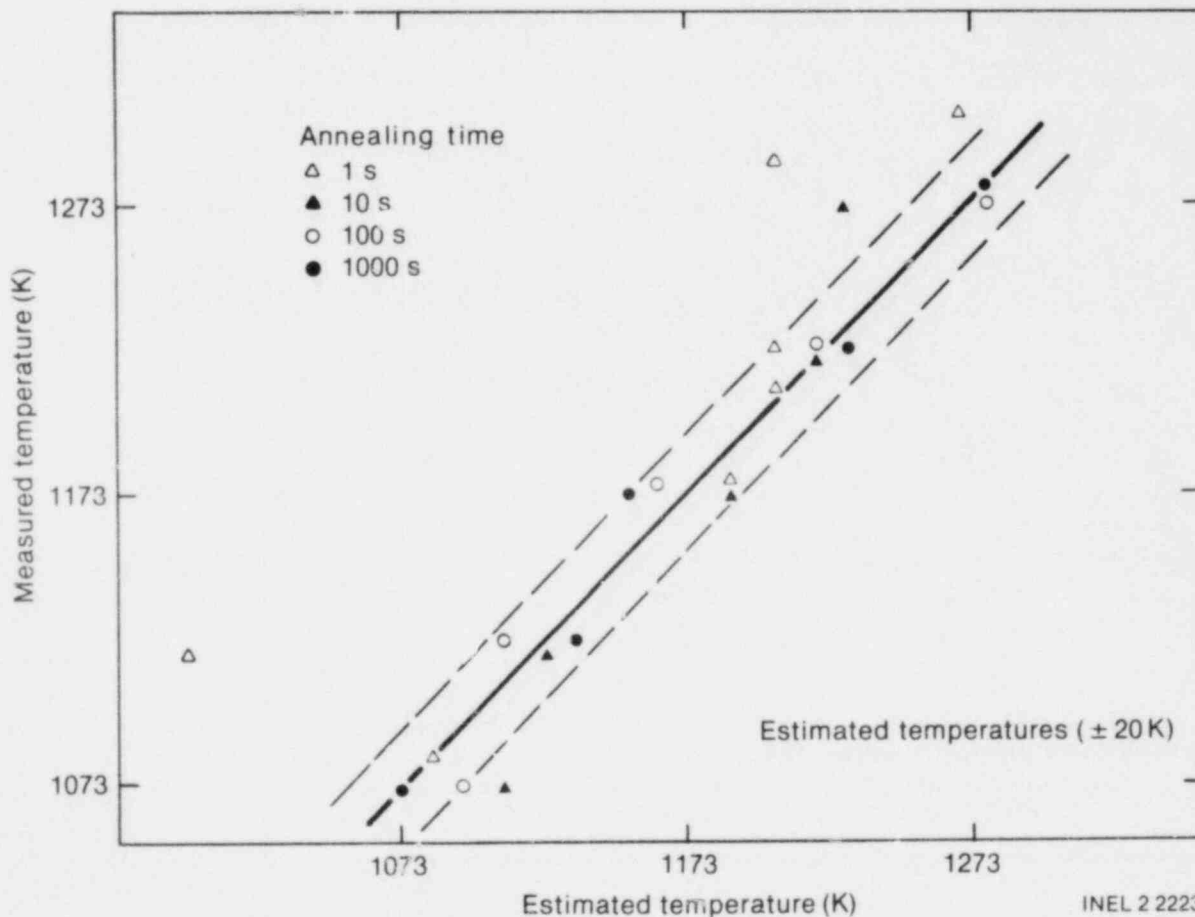

Figure A-15.   Temperature estimates from fraction of α phase in two-phase region.

β **Phase Microstructure.** The β phase microstructures are distinct from either the α or α + β phase microstructures, so the β phase can generally be distinguished from either the α or α + β phases, whereas the α and α + β phases may not always be separated. Figure A-16 shows the microstructure of cladding heated to 1473 K in steam with an unspecified rapid cooling rate to ambient temperature.[A-14] A very sharp circular (almost basket-weave) structure is formed. With slower cooling rates (<2 K/s), a platelet-type structure is formed (Figure A-17).[A-7] A slightly faster cooling rate from the β phase inhibits the precipitation of intermetallics in the grain boundaries. Zircaloy microstructure may be more dependent upon the temperature from which quench is initiated than upon cooling rate. The cooling rate affects the separation between plates and precipitation in the grain boundaries. The differences between the microstructures in Figures A-15 and A-16 may be attributed to differences in cooling rate causing different platelet thicknesses. A change in the β microstructure from a platelet to basket-weave structure was also noted in increasing the cooling rate from 55 to 180 K/min.[A-15]

Figures A-16 and A-17 represent extremes in the β microstructures for wide differences in cooling rates. Only the precipitation of intermetallics in the grain boundaries outline the platelet structure, and with more rapid cooling, the platelets may not be distinguished because of less intermetallic precipitation. Figure A-18 illustrates the effects of even faster cooling rates for a Zr-1.2% Cr-0.1% Fe alloy cooled from 1323 K.[A-16] For cooling rates between 10 and 2000 K/s, the Widemanstatten structure is formed, but for cool-

Figure A-17.   Microstructure of unirradiated zircaloy heated at 1254 K (β phase) for 300 s and slowly cooled.

ing rates 2000 K/s and greater, a Martensitic structure is formed which has fine, acicular grains that are largely unresolvable under the optical microscope. Although this alloy with its high chromium content is atypical of the zircaloy alloy used for LOFT cladding, the microstructures represent the different microstructures for the β phase. Microstructures of the β phase would be needed with cooling rates <1 K/s to ensure that the β microstructure can always be identified, if the actual LOCE cooling rates were <2 K/s.

Dispersed hydrides precipitated from the β phase follow the transformed β phase habit planes and exhibit tangential, oblique, and radial orientations within the prior β phase field.[A-11,A-12] These microstructures may be modified by different cooling rates.

In addition to the basic microstructure of the β phase, another characteristic of the β microstructure after being heated in steam, is the formation of a layer of oxygen-stabilized α zirconium (Figure A-16). The dissolution of oxygen in β zircaloy raises the transition temperatures to a sufficiently high value so that α zirconium is stabilized

Figure A-16.   Cross section of zircaloy-4 tube oxidized in steam at 1473 K (β phase).

31
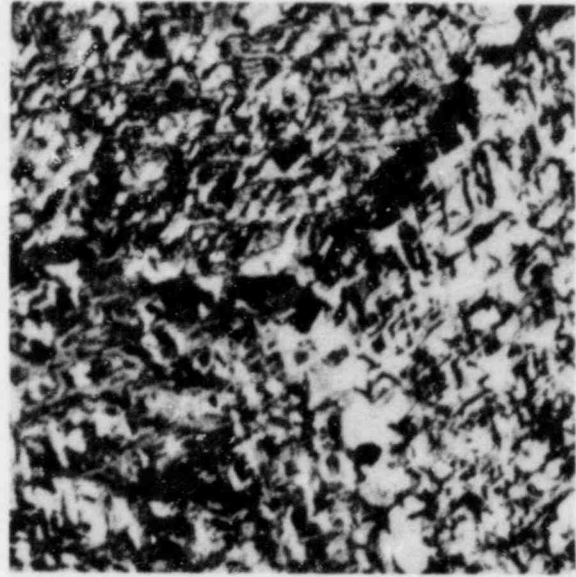
(a) Cooling rate ≈ 20 K/s

(b) Cooling rate ~ 1000 K/s
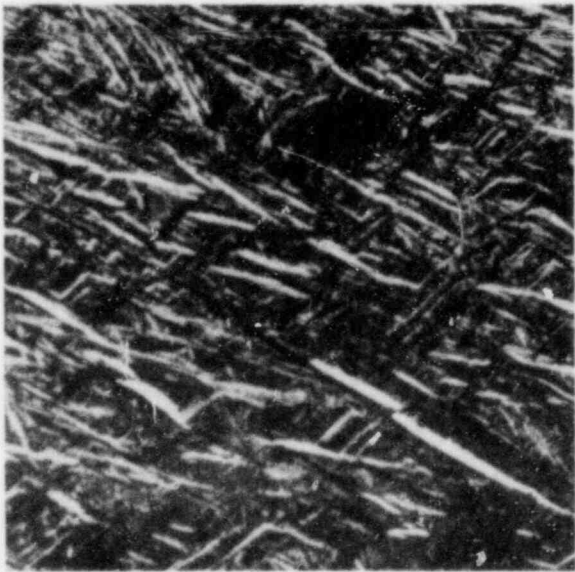
(c) Cooling rate ~ 2000 K/s

(d) Cooling rate ~ 4200 K/s

Figure A-18.   Effect of cooling rate on the microstructure of Zr-1.2 w/o Cr-0.1 w/o Fe alloy cooled from 1323 K (β phase).

in a temperature range in which oxygen-free β zircaloy is normally stable. However, upon cooling to room temperature, the decrease in oxygen solubility causes α zircaloy to precipitate in the β phase adjacent to the oxygen stabilized α layer and a displacement of the stabilized α layer towards the β region.[A-17] This two-phase ($\alpha + \beta$) layer cannot be distinguished from β at high temperatures because of the α phase precipitated in the β region. However, this precipitation only occurs in a narrow region adjacent to the oxygen-stabilized α layer. The remaining metal layer should be characteristic of β zircaloy.

Summary

Zircaloy microstructures and the known transition temperatures provide an excellent independent means to bracket cladding temperatures from postirradiation examination (PIE). Although the present data base is not capable of determining exact temperatures within each phase region, the data base does not preclude new microstructure data from being used to resolve temperatures in the two-phase $\alpha + \beta$ region to within ± 20 K. Because of the potential benefits, the latter proposition needs further exploration to minimize human errors and establish the uncertainties in this method.

In addition to the normal zircaloy alloying elements (tin, iron, chromium, and nickel), oxygen and hydrogen, which can be introduced during a LOCE, also affect zircaloy phase transformation and microstructures. Dissolved oxygen tends to stabilize the α phase and raises the transition temperature for the α to β transformation, whereas dissolved hydrogen is a β phase stabilizer and lowers the transition temperatures. The change in transition temperatures arising from the dissolved hydrogen and oxygen must be taken into account when microstructures are used to estimate temperatures.

The platelet or basket-weave microstructure is sufficient to identify the high-temperature, single-phase β phase and the upper transition temperature. The β phase in the two-phase $\alpha + \beta$ region cannot always be identified to separate the single α phase from the two-phase $\alpha + \beta$ region. These two regions cannot be distinguished with slow cooling except by the redistribution of precipitates, which is also affected by cooling rate. The β phase morphology in the two-phase $\alpha + \beta$ region and the β phase region, as well as the distribution of precipitates in each region, need to be correlated with cooling rates (for LOCE conditions between 1 and 20 K/s) and time at temperature to adequately characterize zircaloy microstructures in a steam atmosphere.

The transition from cold-worked to annealed zircaloy establishes a temperature in the high α phase region which can be used to estimate cladding temperatures. The transition temperature determined from microstructures is 866 K, slightly lower than 922 K determined from microhardness measurements.

References

A-1.   S. L. Seiffert and G. R. Smolik, *Post Irradiation Examinations Results for the Power-Cooling Mismatch Test 2A*, TREE-NUREG-1029, February 1977.

A-2.   M. L. Picklesimer, "Method of Annealing and Rolling Zirconium Base Alloys," U.S. Patent 2,894,866, July 14, 1959.

A-3.   D. O. Hobson, *The Effect of Thermal Transients on The Hardness of Zircaloy Fuel Cladding*, ORNL-NUREG-TM-26, June 1976.

A-4.   E. Gebhardt et al., "Untersuchungen zur Kinetic der Reaction Zwischen Zirkonium und Sauerstoff, sowie uber die Konstition des Systems Zirkonium-Sauerstoff," *Journal Nuclear Materials 4*, 1961, p. 255.

A-5.   R. L. Beck, "Zirconium-Hydrogen Phase System," *Transactions American Society for Metals ASM 55*, 1962, p. 542.

A-6.   S. Seiffert, "The Effect of Hydrogen on the Oxygen Embrittlement of Beta-Quenched Zircaloy-4 Fuel Cladding," *Fifth Conference on Zirconium in the Nuclear Industry*, ASTM STP 754, D. G. Franklin, (ed.), American Society for Testing and Materials, 1981.

A-7.   C. S. Olsen, *Effects of Irradiation Upon Zircaloy Microstructures and Transformation Temperatures*, RE-M-77-010, EG&G Idaho, Inc., September 30, 1977.

A-8.   B. Nath et al., "Effect of Hydrogen Concentration and Cooling Rate on Hydride Precipitation in α-Zirconium," *Journal Nuclear Materials 58*, 1975, pp. 153-162.

A-9.   G. W. Gibson et al., *Characteristics of UO$_2$-Zircaloy Fuel Rod Materials from the Saxton Reactor for Use in the Power Burst Facility*, ANCR-NUREG-1321, September 1976.

A-10.   J. C. Greenbank and S. Harper, "Solute Distribution in Oxidized Zirconium Alloys," *Electrochemical Technology 4*, 1966, p. 142.

A-11.   J. S. Bradbrook et al., "The Precipitation of Zirconium Hybrids in Zirconium and Zircaloy-2," *Journal Nuclear Materials 42*, 1972, pp. 142-160.

A-12.   B. Nath et al., "Effect of Hydrogen Concentration and Cooling Rate on Hydride Precipitation in α-Zirconium", *Journal Nuclear Materials 58*, 1975, pp. 153-162.

A-13.   J. J. Kearns et al., "Effect of Alpha/Beta Phase Constituents of Superplasticity and Strength of Zircaloy-4," *Journal Nuclear Materials 61*, 1976, pp. 169-184.

A-14.   J. V. Cathcart et al., *Zirconium Metal-Water Oxidation Kinetics, Part 4: Reaction Rate Studies*, ORNL-NUREG-17, August 1977.

A-15.   H. M. Chung et al., "Mechanical Properties of Zircaloy Containing Oxygen," *Light-Water-Reactor-Safety Research Program Quarterly Progress Report, January-March 1976*, ANL-76-49, 1976, p. 37.

A-16.   W. M. Rumball, *The Hardenability of Zr-1.2 wt% Cr-0.1 wt% Fe*, AECL 3050, 1968.

A-17.   A. Sawatzky et al., "Oxidation of Zirconium During a High Temperature Transient," *Zirconium in the Nuclear Industry*, ASTM STP 633, 1977.
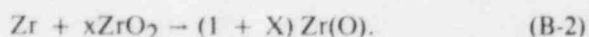
APPENDIX B
ZIRCALOY OXIDATION

APPENDIX B
ZIRCALOY OXIDATION

The chemical reaction of zirconium with steam is commonly depicted by

$$ZrO_2 + 2H_2 \rightarrow Zr + 2H_2O. \tag{B-1}$$
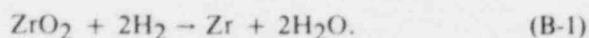
However, zirconium can dissolve up to 30 atomic percent oxygen so that Equation (1) must be modified to reflect the dissolution of oxygen into the base metal;

$$Zr + xZrO_2 \rightarrow (1 + X) Zr(O). \tag{B-2}$$

At temperatures above the $\alpha + \beta/\beta$ transition, sufficient oxygen may be dissolved in the area adjacent to the oxide layer to form an oxygen-stabilized alpha (α) layer in the normally stable beta (β) phase temperature region.[B-1] At lower temperatures an oxygen-rich zone forms adjacent to the oxide layer. The growth of the oxide layer, the oxygen-rich layer, or the total thickness of these layers may be measured or, alternatively, the weight of the oxygen uptake may be measured.

Oxidation kinetics follow an expression of the form:

$$W = ke^{-Q/RT} t^n \tag{B-3}$$

where

W $=$ weight gain or oxide thickness, ect.

k $=$ a constant

Q $=$ activation energy

R $=$ gas constant

T $=$ temperature (K)

t $=$ exposure time

n $=$ a constant dependent upon the rate law ($n = 1/3$ for cubic and $1/2$ for parabolic kinetics).

The layer thickness, but not the weight gain, is usually measured during postirradiation examination (PIE) after a fuel rod is removed from the reactor.

In the following sections, the literature on the oxidation kinetics of zircaloy with steam is reviewed to evaluate the constants k, Q, and n in the above equation for weight gain and oxide layer thicknesses. The review is categorized with regard to (a) temperatures above 1770 K, (b) temperatures between 1270 and 1770 K, and (c) temperatures between 970 and 1270 K.

Temperatures Above 1770 K

Baker-Just[B-2] had one data point, took data from Bostrom[B-3] and Lemmon[B-4] and derived the following equation from these data at the zircaloy melting point:

$$W^2 = 3.36 \times 10^7 e^{-45,500/RT} t \tag{B-4}$$

where W is the weight of zirconium reacted (g/cm^2); the other terms have been defined above.

The data base for this correlation is based on the reaction of molten zircaloy with steam, and results in oxidation rates about a factor of two higher than that from Cathcart's equations discussed below. Oxidation extent determined from hydrogen release from SPERT tests with molten zircaloy agrees within $\pm 10\%$ of values predicted from the Baker-Just Equation (Table B-1). The data base for the Baker-Just equation and the agreement of the equation with the SPERT data show that this equation is only applicable for molten zircaloy and is not necessarily valid at lower temperatures.

Temperature between 1270 and 1770 K

Cathcart[B-5] determined the oxidation kinetics of zircaloy between 1273 and 1773 K in steam. From metallographic examinations of the oxidized samples, he measured the thicknesses of the oxide, oxygen-stabilized α, and oxide plus oxygen-stabilized α layers. The total oxygen uptake was evaluated from these thicknesses using a computer program that calculates the oxygen distribution. In these experiments, particular care was taken to obtain thickness measurements at the points where

Table B-1. Comparison of calculated and measured extent of the zirconium-water reaction from CDC tests

Test	Maximum Cladding (K)	Predicted Baker-Just	Measured Hydrogen-Release	Deviation from Measured Value (%)
537	1816	16.39	14.50	+13.0
539	1962	39.49	32.37	+22.0
545	1978	35.00	37.48	-6.6
Average	—	—	—	+9.7

very precise temperature measurements were made. The layer thicknesses and oxygen uptake followed the parabolic (second order) oxidation kinetics given by:

$$\frac{dW}{dt} = \delta^2/2W \tag{B-5}$$

where W represents the oxide, α, or oxide plus α thicknesses or the oxygen uptake. The term $\delta^2/2$ represents the parabolic reaction rate constant which is given for oxide, α, oxide plus α lay and oxygen pickup by the next four equations, respectively:

$$\frac{\delta_\phi^2}{2} = 0.01126$$

$$\binom{+30\%}{-23\%} \exp\left[-35890(\pm 2.2\%)/RT\right] \text{ cm}^2/\text{s} \tag{B-6}$$

$$\frac{\delta_\alpha^2}{2} = 0.7615$$

$$\binom{+54\%}{-35\%} \exp\left[-48140(\pm 2.6\%)/RT\right] \text{ cm}^2/\text{s} \tag{B-7}$$

$$\frac{\delta_\xi^2}{2} = 0.3412$$

$$\binom{+17\%}{-15\%} \exp\left[-41700(\pm 1.2\%)/RT\right] \text{ cm}^2/\text{s} \tag{B-8}$$

$$\frac{\delta_\tau^2}{2} = 0.1811$$

$$\binom{+20\%}{-16\%} \exp\left[-39940(\pm 1.4\%)/RT\right]$$

$$(\text{g/cm}^2)^2/\text{s}. \tag{B-9}$$

The quantities in the brackets refer to the individual 90% confidence limits on the pre-exponential and activation energy terms.

Biederman et al.,[B-6] also measured oxidation kinetics between 1255 and 1755 K in atmospheric steam and used metallography as the principal tool to determine reaction layer thicknesses. The following expression was obtained by Biederman for the thickness of the oxide and oxygen-stabilized α layer:[B-6]

$$\frac{\xi^2}{2} = 0.02244 \exp(-33,620/RT) \text{ (cm}^2/\text{s)} \tag{B-10}$$

and for total oxygen uptake:

$$\frac{\delta_\tau^2}{2} = 0.01907 \exp(-33,370/RT)(\text{mg/cm}^2)^2/\text{s}. \tag{B-11}$$

Biederman's equations result in oxidation rates approximately a factor of two less than Cathcart's at 1733 K.

The lack of agreement between Biederman and Cathcart may be attributed to poor temperature measurements during Biederman's experiments because of different power generation in the electrically heated cladding at the grooved thermocouple location.

During transient heating for a double-peak blowdown temperature-time curve, oxidation during the first peak was found to reduce the amount of oxidation during subsequent heating during reflood.[B-6] Similar behavior was found by Cathcart.[B-5] For example, one sample was heated to 1673 K, cooled to 923 K, and reheated to a peak temperature of 1323 K. For this transient, the observed oxide thickness was 12.6 μm compared with a calculated value of 27.2 μm, a discrepancy of 116%. The samples that exhibited significant differences between the observed and calculated oxide thickness values exhibited the common features that (a) a two-peak transient was involved, and (b) the temperature of the second peak was < 1473 K.

The monoclinic to tetragonal phase transformation in the zirconium dioxide was thought to be the cause for this discrepancy. Due to the hysteresis of the transformation of the oxide and effects of crystallite size upon the transformation, the transformation takes place over a narrow temperature range near 1473 K upon heating, but upon cooling the transformation starts at 1273 K and is not completed until several hundred degrees lower. The smaller oxidation extent during the second transient arises from a slower mass flux through a monoclinic oxide transformed at a much lower temperature from the higher temperature tetragonal oxide.

Leistikow[B-7] measured the reaction of zircaloy with steam from 973 to 1573 K for times up to 15 min. The samples were heated inductively in a tube furnace and the reaction layer thicknesses were measured from metallographic examination. The weight gain measurements were then calculated from these reaction layer thicknesses.

The oxidation kinetics below 1273 K exhibited increasingly cubic kinetics (described below) as the temperature decreased, but parabolic kinetics

were selected with the following equations to represent the entire temperature region from 973 to 1573 K:

$$X_\xi = 1.29 \ t \exp(-11{,}043/T) \ (cm) \qquad (B-12)$$

where X_ξ is the oxide plus α thickness;

$$W = 0.724 \ t \exp(-10{,}481/T) \ (g/cm^2) \qquad (B-13)$$

where W is the weight gain.

Oxidation Between 970 and 1270 K

The time exponents from Leistikow's low-temperature oxidation data[B-7] were combined with those from Pawel[B-8] determined from measurements in high-pressure steam. The time exponents are listed in Table B-2. The exponents for Leistikow's data vary from 0.32 to 0.35 (three values) and between 0.38 and 0.39 (three values) and at 1273 K, the time exponent was 0.45. For temperatures at 1229 K and lower and pressure between atmospheric and 3.45 MPa, the time exponents indicate that the zircaloy oxidation

Table B-2. Exponents on time derived from Leistikow[B-7] and ORNL data[B-8]

Temperature (K)	Pressure (MPa)	Exponent	Reference
973	0.1	0.343	B-7
1023	0.1	0.391	B-7
1073	0.1	0.316	B-7
1123	0.1	0.382	B-7
1173	0.1	0.353	B-7
1178	0.1	0.295	B-8
1178	3.45	0.372	B-8
1178	6.90	0.356	B-8
1178	10.34	0.545	B-8
1223	0.1	0.399	B-7
1229	0.1	0.309	B-8
1273	0.1	0.446	B-7
1278	0.1	0.461	B-7

kinetics are cubic. A change to parabolic kinetics was indicated at 10.34 MPa and 1178 K. Pawel reported that the oxidation rates increased with increasing pressure, and the kinetics were non-parabolic. The data in Table B-2 show that the kinetics are cubic up to 6.90 MPa, but revert to parabolic kinetics at 10.34 MPa. Cubic behavior at extremely low oxygen or steam pressures was also determined by M. Leclercq.[B-9]

Urbanic[B-10] measured the extent of reaction of zircaloy with steam in the temperature range from 873 to 1223 K and for times to 27,600 s to determine the effects of the α/β transformation upon the oxidation kinetics. Oxygen weight gain was determined from pre- and posttest weight measurements.

For short times, parabolic kinetics were identified, but the results changed for longer times to linear kinetics. The parabolic reaction rate constants were represented by two different equations in order to be consistent with existing AECL data below 873 K and above 1223 K.

$$W^2 = 2.02 \times 10^6 \exp(-31,821/RT)$$

$$t\,(g/m^2)^2 \quad T \leq 1103 \text{ K} \tag{B-14}$$

$$W^2 = 1.56 \times 10^{10} \exp(-51,593/RT)$$

$$t\,(g/m^2 \quad T > 1103 \text{ K}. \tag{B-15}$$

The data were separated by the $\alpha/\alpha + \beta$ transition into two equations.

Biederman[B-11] measured the isothermal oxidation of zirconium in steam between 922 and 1255 K. At temperatures above 1158 K, two layers in the room temperature microstructures were observed: the oxide layer, and an oxygen-rich zone. In the $\alpha\ \beta$ transition region, the parabolic growth of the oxide and the oxygen-rich layers was irregular in comparison with the planar interfaces typically found for oxidation above the α/β transformation.

At temperatures below 1158 K, only an oxide layer was observed. Some tendency toward non-parabolic behavior was observed at low temperatures and long durations, but this deviation was small and of an order of magnitude in the data scatter.

Biederman erroneously separated the oxidation kinetics into the α phase and $\alpha + \beta$ phase at 1158 K. The actual transition temperature is 1103 K. The following two equations were used, as with Urbanic, to represent the growth of the outside oxide layer.

$$x = 203.2\ t^{1/2} \exp(-27,800/R)\ T \leq 1158 \text{ K}$$

$$\tag{B-16}$$

$$X = 2.2 \times 10^5\ t^{1/2} \exp(-12,050/R)$$

$$T > 1158 \text{ K}. \tag{B-17}$$

Summary

The rate constants for parabolic oxide growth rates are summarized in Figure B-1 for temperatures above 970 K. The reaction rate is also shown for the intermediate temperatures for comparison with ORNL and Leistikow high-temperature parabolic rates and the Biederman low-temperature rates.

The oxidation kinetics may be conveniently divided into two temperature regimes corresponding to the zircaloy phase regions: an intermediate temperature range in which α or $\alpha + \beta$ phases exist, and the high-temperature range in which only β phase exists. The $\alpha/\alpha + \beta$ transition temperature also corresponds to the tetragonal to monoclinic oxide transformation upon cooling. The differences in rates near 1270 K may be due not only to the zircaloy microstructure, but to the type of oxide formed, as well.
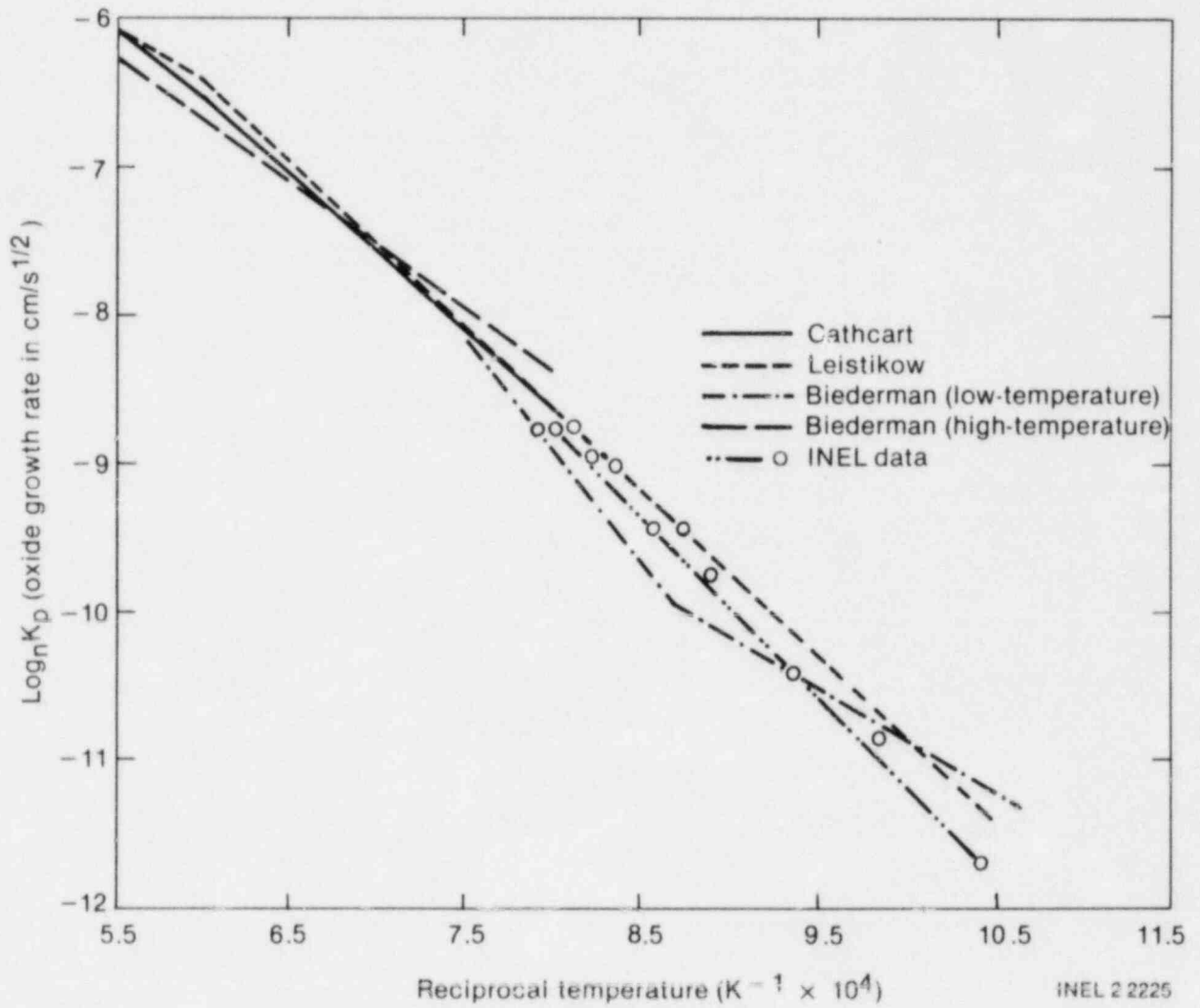
Figure B-1.   Summary of oxidation kinetics for high and intermediate temperatures.

41

References

B-1. E. Gebhardt et al., "Untersuchungen zur Kinetic des Reaction Zevischen Zirkonium und Sauerstoff, Sowic uber die Konstitcon des Systems Zirkonium-Sauerstoff," *Journal Nuclear Materials, 4*, 1961, p. 255.

B-2. L. Baker Jr. and L. C. Just, *Studies of Metal-Water Reactions at High Temperature, Part 3: Experimental and Theoretical Studies of the Zirconium-Water Reactions*, ANL-6548, May 1962.

B-3. W. A. Bostrom, *The High Temperature Oxidation of Zircaloy in Water*, WAPD-104, March 19, 1954.

B-4. A. W. Lemmon Jr., *Studies Relating to the Reaction Between Zirconium and Water at High Temperature*, GMI-1154, January 8, 1957.

B-5. J. V. Cathcart et al., *Zirconium Metal-Water Oxidation Kinetics, Part 4: Reaction Rate Studies*, ORNL-NUREG-17, August 1977.

B-6. R. Biederman et al., *A Study of Zircaloy-4-Steam Oxidation Reaction Kinetics*, EPRI NP-225 (PB 260 693), September 1976.

B-7. S. Leistikow et al., "Kinetik und Morphologie der Isotherm Damp-Oxidation von Zircaloy-4 bei 700-1300°C," KFK-2587, March 1978.

B-8. R. E. Pawel et al., *Zirconium Metal-Water Oxidation Kinetics V. Oxidation of Zircaloy in High Pressure Steam*, ORNL-NUREG-31, December 1977.

B-9. M. Leclercq, *Contribution a L'Etude du Mecanism D'Oxydation du Zirconium Par ou Allie par L'Oxygene et La Vapeur D'Eau*, EUR 4507, 1970.

B-10. V. Urbanic, private communication, February 1979.

B-11. R. R. Biederman et al., "A Study of Zircaloy Steam Oxidation Reaction Kinetics," *First Interim Progress Report July 1, 1976 Through October 15, 1976*, Project No. RP 249-2, October 1976.

APPENDIX C
ANALYSIS OF TEMPERATURE ERRORS
FROM OXIDATION KINETICS

APPENDIX C
ANALYSIS OF TEMPERATURE ERRORS
FROM OXIDATION KINETICS

Linear error propagation techniques were used to evaluate the errors in temperatures derived from measurements of oxide thickness, time at temperature, and an analytical expression for the oxidation kinetics. The basic procedure is to perturbate each parameter and calculate the change in temperature resulting from each parametric perturbation. The overall error in temperature is then determined from the following equation:

$$\Delta T = \sum_{i=1}^{n} (\partial T/\partial P_i)^2 \, \sigma_i^2 \qquad \text{(C-1)}$$

where

n = number of parameters

σ_i = standard deviation in the ith parameter

∂T = change in temperature

∂P_i = perturbation in the ith parameter.

The relative contribution from each parameter is determined from the following equation:

$$CON_i = \frac{(\partial T/\partial P_i)^2 \, \delta_i^2}{\displaystyle\sum_{i=1}^{n} (\partial T/\partial P_i)^2 \, \delta_i^2} \qquad \text{(C-2)}$$

where CON_i is the contribution from the ith parameter; the other terms are defined above.

Errors from High-Temperature Kinetics

Equations (C-3) and (C-4) from Cathcart were used to evaluate errors in isothermal temperature estimates from measurements of thickness measurements of the oxide plus α layer and oxygen uptake using linear error propagation techniques. The errors in Equations (C-3) and

(C-4) were reduced to 1-σ values and the error (1-σ) in the oxide plus α layer thickness or oxygen uptake was assumed to be 10%, and the error in the time at temperature was assumed to be ±5% (1-σ). With linear error propagation, the relative contribution from each parameter to the total error was also determined.

$$X^2 = 0.6824 \begin{pmatrix} +17\% \\ -15\% \end{pmatrix} \exp \frac{-41700 \, (\pm 1.2\%)}{RT} \, t$$

$$\text{(C-3)}$$

$$W^2 = 0.3622 \begin{pmatrix} +20\% \\ -16\% \end{pmatrix} \exp \frac{-39940 \, (\pm 1.4\%)}{RT} \, t$$

$$\text{(C-4)}$$

where

T = temperature (K)

R = 1.987 (cal/mole·K)

X = thickness of the oxide plus α layer (cm)

W = total oxygen weight gain (g/cm^2).

The quantities appearing in the brackets of the above equations refer to the individual 90% confidence limits on the pre-exponential and activation energy terms.

The results of these calculations are summarized in Tables C-1 and C-2 for Equations (C-3) and (C-4), respectively. For Equation (C-3) or (C-4), the error (based upon 1-σ) varies from about 20 K at 1273 K to about 38 K at 1773 K. The percentage error does not vary as much as the absolute error and has an average value of 1.75% for Equation (C-3) and an average of 1.91% for Equation (C-4). Assuming a 95% confidence level for the error in cladding temperature, Equation (C-3) results in a error of ±38 K at 1273 K and an error of ±69 K at 1773 K, and Equation (C-4) results in an error of ±41 K at 1273 K and ±75 K at 1773 K. Because oxide plus α layer thicknesses will be measured, the applicable random error is estimated between ±38 and ±69 K for temperatures above 1273 K.

45

Table C-1. Temperature errors and relative contribution for oxide plus α thicknesses [Equation (C-3)]

Temperature (K)	Error (1-σ)		Relative Contribution (Fraction)			
	K	%	Energy	Preexponential Constant	Time	Thickness
1273	19.3	1.52	0.2320	0.1343	0.0379	0.5959
1373	22.1	1.61	0.2059	0.1385	0.0391	0.6164
1473	25.1	1.70	0.1837	0.1420	0.0402	0.6341
1573	28.3	1.80	0.1647	0.1450	0.0410	0.6449
1673	31.7	1.89	0.1483	0.1474	0.0418	0.6626
1773	35.0	1.97	0.1341	0.1495	0.0424	0.6741

Table C-2. Temperature errors and relative contribution for total oxygen absorption [Equation (C-4)]

Temperature (K)	Error (1-σ)		Relative Contribution (Fraction)			
	K	%	Energy	Preexponential Constant	Time	Thickness
1273	21.1	1.66	0.2619	0.1622	0.0344	0.5414
1373	24.2	1.76	0.2336	0.1680	0.0357	0.5628
1473	27.4	1.86	0.2092	0.1729	0.0368	0.5812
1573	30.8	1.96	0.1881	0.1770	0.0377	0.5972
1673	34.5	2.06	0.1699	0.1805	0.0385	0.6112
1773	38.4	2.17	0.1540	0.1834	0.0391	0.6235

Analysis of the relative error from each individual parameter shows that errors in time are not significant and the errors in thickness measurement are about the same as that from the combined errors of the energy term and preexponential constant. The last two terms were determined to the limits of kinetic data measurement, so the only feasible improvement is measurement of the layer thickness. The 10% error assumed here represents a probable value expected with the use of photomicrographs.

Errors from Intermediate-Temperature Kinetics

The temperature errors from Equations (C-5) and (C-6) from the INEL data were evaluated using the 1-σ errors listed and assuming a 10% error in weight gain and oxide thickness measurements and a 5% error in time. The results of these calculations are summarized in Tables C-3 and C-4. The estimated errors in temperature

using weight gain measurements vary from ±30.6 K at 973 K to ±43.4 K at 1223 K, whereas those from oxide thicknesses vary from 39.9 K at 973 K to 55.8 K at 1223 K. The average percentage error for oxide growth is 4.3%. The corresponding 95% confidence level is ±78 K at 923 K and ±109 K at 1223 K. Between 89 and 91% of the temperature error from oxide thickness originates with the uncertainties in the constants in Equation (C-6) compared with about 40% using the high temperature Equation (C-3).

$$W = 479.02 \begin{pmatrix} +23\% \\ -29\% \end{pmatrix} \exp \frac{20,400\ (\pm 2.3\%)}{RT}\ t^{1/2}$$

(C-5)

$$X = 2.526 \times 10^4 \begin{pmatrix} +39\% \\ -28\% \end{pmatrix}$$

$$\exp \frac{-23,920\ (\pm 3.1\%)}{RT}\ t^{1/2}$$

(C-6)

where

W = weight gain (mg/cm^2)

T = temperature (K)

R = 1.987 (cal/mole·K)

X = oxide thickness (micrometers).

The estimated errors in the layer thickness measurements are slightly worse than the errors in oxygen uptake, primarily as a result of higher uncertainty in the constants in the rate equations and a larger contribution to the uncertainty from these constants.

Summary

The temperature errors resulting from the high-temperature oxidation kinetics of Cathcart and the measurement of the thickness of oxide plus oxygen-stabilized α layer results in a random error of 38 to 69 K based upon a 95% confidence level. Most of the error is attributed to the measurement of the reaction layers. The Cathcart equation needs no further improvement and offers the best representation for deducing temperatures from measurements of reaction layers. The only improvement that may be required is in the thickness measurements of the oxide layer.

However, for intermediate temperatures between 973 and 1273 K, the oxidation kinetics are not quite as good as the high-temperature oxidation kinetics. The uncertainty in the temperature estimates are between ±78 and ±109 K, with most of the error involving the constants in the equation for the reaction kinetics. Although improvements appear to be needed in the uncertainties in the constants, improvements in resolution of the oxide layer boundaries would also be required.

Table C-3. Temperature errors and relative contribution for oxygen absorption at intermediate temperatures [Equation (C-5)]

Temperature (K)	Error (1-σ) K	Error (1-σ) %	Relative Contribution (Fraction) Energy	Relative Contribution (Fraction) Preexponential Constant	Relative Contribution (Fraction) Time	Relative Contribution (Fraction) Thickness
973	30.6	3.14	0.5292	0.3816	0.0054	0.0839
1023	33.0	3.23	0.5046	0.4013	.0057	0.0885
1073	35.4	3.30	0.4810	0.4201	0.0059	0.0929
1123	38.0	3.38	0.4588	0.4379	0.0620	0.0971
1173	40.6	3.46	0.4376	0.4548	0.0065	0.1012
1223	43.4	3.55	0.4175	0.4708	0.0067	0.1050

Table C-4. Temperature errors and relative contribution for oxide thickness at intermediate temperatures [Equation (C-6)]

Temperature (K)	Error (1-σ)		Relative Contribution (Fraction)			
	K	%	Energy	Preexponential Constant	Time	Thickness
973	39.9	4.10	0.5691	0.3926	0.0023	0.0359
1023	42.8	4.18	0.5450	0.4145	0.0024	0.0381
1073	45.9	4.28	0.5218	0.4355	0.0026	0.0401
1123	49.1	4.37	0.4997	0.4555	0.0027	0.0421
1173	52.4	4.47	0.4785	0.4747	0.0028	0.0441
1223	55.8	4.56	0.4583	0.4929	0.0029	0.0459

EG&G Idaho, Inc.
P.O. Box 1625
Idaho Falls, Idaho 83415